

https://dspace.org/

Test beam campaigns for readout electronics of the upgrade Tile Calorimeter of the ATLAS Detector

Lekalakala, Nthabiseng Miranda

2020

https://hdl.handle.net/10539/31022

Downloaded from a DSpace repository. https://dspace.org/

Test beam campaigns for readout electronics of the upgrade Tile Calorimeter of the ATLAS Detector



Nthabiseng Miranda Lekalakala

University of the Witwatersrand

Supervisor

Bruce Mellado

In partial fulfillment of the requirements for the degree of

Master of Science in Physics

Acknowledgements

I would like to honor the South Africa - CERN Collaboration (SA-CERN), the South African Nuclear Human Assets Research Program (SAHARP) and the National Research Foundation (NRF) for their financial assistance. The opinions and the findings expressed in this document are the views of the author and shall not necessarily be attributed to the SA-CERN, SANHARP or the NRF. A special thanks to Tamar Zakareishvili, a fellow TileCal colleague who helped me with the analysis of the Test-Beam data and also Priscilla Pani who provided the initial code for the electron analysis. I would also like to thank Jalal Abdallah who has mentored me during my work on the DVS system and also on the Tile demonstrator assembly. I would also like to thank Irakli Minashvili and the whole Tile Calorimeter group for their guidance during my stay at CERN and assistance during the tasks I was given.

I would like to thank my Wits University colleagues especially Thabo Masuku and Kgomotso Monnakgotla for their help during the writing of this thesis. I would not have been able to finish this thesis without their help. I would also like to thank grandfather who passed away during the beginning of my stay at CERN and very sad I could not attend his funeral. May his soul rest in peace.

Special thanks goes out to my supervisor Bruce Mellado for giving

me this opportunity of doing my research at CERN. I would like also thank him for his mentorship throughout this research.

DECLARATION

I declare that this Thesis is the product of my own research, except where there is explicit reference to other people's work. It is being submitted to the University of Witwatersrand, Johannesburg, for the Degree of Master of Science. It was not submitted at any other university before for any qualification or examination.



6 November 2020

Nthabiseng Miranda Lekalakala | Date

Abstract

The TileCal is a sampling calorimeter that resides in the inner part of the ATLAS detector and it is used to measure energies carried by charged and neutral particles. The LHC plans to increase the current luminosity to High Luminosity LHC, which will create more opportunities in the search for physics beyond the Standard Model. This increase in luminosity, with almost an order of magnitude above the original design, will result in an increase in the corresponding particle fluxes in the detector, and this will require a major upgrade of all the ATLAS detector systems. The increase in the number of collisions per bunch crossing will cause deterioration in the performance of the ATLAS detector. However, an upgrade in the readout electronics of the calorimeter, together with other upgrades in the inner tracker, trigger system and muon spectrometer will improve performance. The Test-Beam (TB) aims to test the performance of the proposed new electronics for the forthcoming TileCal upgrades. The results obtained from TB are compared with the results of the current electronics, and conclusions on new electronics are drawn on the basis of correspondence between the new and old electronics. The results of the analysis carried out in this thesis show that the TB data corresponds to the simulated data and that of the old electronics.

List of Publications

Published Journal Article:

- V. Baranov, Yu.I. Davydov, R. Erasmus, C.O. Kureba, N. Lekalakala, T. Masuku, J.E. Mdhluli, B. Mellado, G. Mokgatitswane, E. Sideras-Haddad, I. Vasilyev and P.N. Zhmurin, "*Effects of the neutron radiation on the optical and structural properties of blue and green emitting plastic scintillators*", Nuclear Inst. and Methods in Physics Research B vol 436, December 2018.

Published Proceedings:

- N. Lekalakala, T. Masuku and B. Mellado, "*The Diagnostic and Verification System for the Tile Calorimeter Trigger and Data Acquisition framework of the ATLAS Detector*", Submitted to Proceedings of SAIP2019, 64^{th} Annual Conference of the South African Institute of Physics, July 2019; Polokwane, South Africa.

- N. Lekalakala, T. Masuku and B. Mellado, "*Overview of test beam campaigns for readout electronics of the upgrade Tile Calorimeter of the ATLAS Detector*", To appear in the book of Proceedings of HEPP2019, the High Energy Particle Physics workshop, February 2019; Port Elizabeth, South Africa.

- G. Mokgatitwane, B. Mellado, E. Sideras-Haddad, R. Erasmus, T. Masuku, J.E Mdhuli, N. Lekalakala, C.O Kureba, L. Mashishi, G. Peters and T. Sechogela", *A systematic study of the properties of proton induced damage in plastic scintillators for the upgrade of the Tile Calorimeter of the ATLAS detector*", To appear in the book of Proceedings of HEPP2019, the High

Energy Particle Physics workshop, February 2019; Port Elizabeth, South Africa.

Contents

List of Publications v

1 Introduction **1**

1.1 Motivation 2

1.2 Overview of the Thesis 3

2 The ATLAS Detector of the LHC **4**

2.1 The Large Hadron Collider 4

2.2 The ATLAS Detector 6

2.3 Components of the ATLAS Detector 8

2.3.1 The Inner Detector 8

2.3.1.1 The Pixel Detector 9

2.3.1.2 The Semi-Conductor Tracker 10

2.3.1.3 The Transition Radiation Tracker 10

2.3.2 The Calorimeters 11

2.3.2.1 Electromagnetic Calorimeters 11

2.3.2.2 The Hadronic Calorimeters 12

2.3.2.3 The Forward Calorimeters 15

2.3.3 The Muon Spectrometer 16

2.3.4 The Magnet System 17

2.4 The ATLAS Trigger and Data Acquisition Systems 19

2.4.1 The Level-1 Trigger 20
2.4.2 The High-Level Trigger 22

3 The Tile Calorimeter **24**
3.1 The TileCal Front-End Electronics System 26
3.1.1 The Mother-board 26
3.1.2 The Interface Board 26
3.1.3 The Digitiser-Board 27
3.1.4 Photo-Multiplier Tube Block 27
3.1.5 Adder Boards 29
3.2 The TileCal Back-End Electronics System 30
3.2.1 Trigger Timing and Control Module Crates 31
3.2.2 Shaft Module, TTC Receiver in PMC Form Factor, Trigger and ROD busy 31
3.2.3 Laser Readout Driver and Readout Driver 32
3.3 The Calibration Systems 32
3.3.1 The Charge Injection System 32
3.3.2 The Laser System 33
3.3.3 Cesium System 34

4 The Online Software **35**
4.1 The ATLAS Online Software 35
4.2 The TileCal Online Software 38
4.3 The Diagnostics and Verification System 40
4.3.1 DVS Tests 42
4.3.2 Future Plans with DVS 45

5 Requirements for the HL-LHC **48**
5.1 The Trigger and Data Acquisition System 49

5.2 Radiation Hardness 53
5.3 Accessibility to the Electronics 57
5.4 The Reliability and Redundancy 58
5.5 The Optics Robustness and PMT stability 60
5.6 Mechanics 61
5.6.1 The Mini-drawers and Installation 61
5.6.2 The On-detector Electronics 62
5.6.3 The Low and High Voltage Power Supplies 65
5.6.4 Off-detector Electronics 66
5.6.5 The TileCal Demonstrator 68
5.6.6 Calibration Systems 71
5.6.6.1 The Charge Injection System 71
5.6.6.2 The Laser System 71
5.6.6.3 Cesium System 71

6 Test-Beam Campaigns **72**
6.1 Test-Beam Setup 72
6.1.1 Beam Line and Calorimeter setup 73
6.2 Test-Beam Results 75
6.2.1 Results with electrons 75
6.2.2 Results with Muons 83
6.2.3 Performance of the FE electronics 89

7 Conclusions **90**

References **98**

List of Figures

2.1 The LHC Accelerator ring. 6
2.2 The ATLAS Detector. 7
2.3 The ATLAS Inner Detector. 9
2.4 The ATLAS Calorimeter. 12
2.5 Liquid Argon Calorimeter. 13
2.6 The Tile Calorimeter. 14
2.7 The TileCal Cells distribution. 14
2.8 Forward Calorimeter modules. 15
2.9 The ATLAS Muon Spectrometer. 17
2.10 The Magnet System of ATLAS. 18
2.11 The TDAQ system. 20
2.12 The Level-1 trigger. 21
2.13 High Level Trigger. 23

3.1 The Calorimetry sytem. 25
3.2 The Digitiser system. 28
3.3 The Photo-multiplier tube block. 29
3.4 The Back-end partitions. 30

4.1 The partition. 37
4.2 The ROD Crate DAQ. 39

4.3 The TileCal Super-drawer. 41
4.4 The DVS internal architecture 43
4.5 Charge Injection Scan plots for EBA16 in both Low and High Gains. 44
4.6 Results for the high and low frequency noise pedestal tests in every channel. 46

5.1 HL-LHC Timeline 49
5.2 The Trigger system for the upgrades. 50
5.3 Schematic of the signal and data path for the upgraded TileCal. . 51
5.4 Total ionization dose for the upgrades. 54
5.5 Neutron fluence. 55
5.6 Hadron fluence. 56
5.7 The readout electronics for the current system. 58
5.8 The readout electronics for the upgrade system. 59
5.9 The Main-board. 63
5.10 The Daughter-board. 63
5.11 The TileCal and the on-detector drawers. 64
5.12 The PMT assembly. 64
5.13 Block diagram for the back-end electronics of the upgrade system. 67
5.14 The TileCal demonstrator. 69
5.15 The Front-end electronics for the proposed for the upgrades. . . . 70

6.1 The modules and beam elements at the SPS H8 beam-line. 74
6.2 The scanning table at the H8 beam-line. 74
6.3 Beam Profiles for 20 GeV (a), 50 GeV (b) and 100 GeV (c) electron signals. The data for the plots is from the 2018 TB campaigns. . . 76
6.4 C_{long} versus C_{tot}. 78

6.5 The C_{long} (a) plot distribution for the electron signal at 20 GeV (a), 50 GeV (b) and 100 GeV (c). 79
6.6 The C_{tot} plot distribution for the electron signal at 20 GeV (a), 50 GeV (b) and 100 GeV (c). 80
6.7 The simulated results of electrons. 81
6.8 Pure Electron signal plots at 20 GeV (a), 50 GeV (b) and 100 GeV (c) after separation from other particles. 82
6.9 The oscillation of the electron response by the difference in the sample fractions determined by 20 GeV (a), 50 GeV and 100 GeV beam signal. The line indicates the correction for the consequence of Equation 6.3. 84
6.10 Calibration constant from pC to GeV represented as E_{fit}/E_{beam}, for electron beam energies of 20 GeV, 50 GeV and 100 GeV. . . . 85
6.11 The two plots (a) and (b) show the beam response in chambers 1 and 2 for 165 GeV muons. They show how the beam is distributed in each chamber. The bottom plots show the beam at the impact point. 86
6.12 The two plots (a) and (b) at the top shows the beam response in chambers 1 and 2 for the 300 GeV muons. They show how the beam is distributed in each chamber. The bottom plots (c) and (d) shows the beam at the point of impact. 87
6.13 The simulated data of the muons. 88

List of Tables

5.1 Comparison of the present (ROD) and the PPR upgrade architectures of the TileCal BE readout. The redundancy and backup data links are not included. The system has a total number of fibers twice that indicated here. 52
5.2 Simulated radiation doses for 4 ab^{-1} of HL-LHC running. 54
5.3 Safety factors multipliers for radiation certification of ATLAS electronics. 57

Chapter 1

Introduction

The Large Hadron Collider (LHC) is the world's largest particle accelerator, and it is located between Switzerland and France. It was designed to collide particles at a 14 Tev center of mass energy and with a luminosity of 10^{34} $cm^{-2}s^{-1}$ [1]. It consists of a number of experiments that work independently. Two of them, the ATLAS and CMS experiments, have been specifically designed for proton-proton probing. The ATLAS detector consists of a number of sub-detectors, one of which is the Tile Calorimeter (TileCal) designed for the measurement of hadrons. The TileCal is a sampling hadronic calorimeter covering the most central region of the ATLAS experiment. The TileCal detector is made of steel absorber plates and plastic scintillator tiles and is divided into three cylindrical sections along the beam axis: the central Long Barrel (LB) which is subdivided into Long Barrel A (LBA) and Long Barrel C (LBC) and the Extended Barrel (EB) which is subdivided into Extended Barrel A (EBA) and Extended Barrel C (EBC). Each barrel consists of 64 modules divided into groups of tiles called cells. The Photo-Multiplier Tubes (PMTs) and the on-detector electronics used to read the cells are located in the outermost portion of the modules, called the super-drawers. There are a total of 256 super-drawers in the TileCal consisting of $\sim$10000 readout channels [2].

The light produced by the charged particles passes through the plastic scintillator and is collected by Wavelength Shifting fibers (WLS) and then transmitted to the PMTs. The analog signals produced by the PMT are converted to electrical signals and digitised by the on-detector electronics every 25 ns, while an analog sum of the cells in projective towers from the interaction point is transferred to the Level-1 (L1) trigger system for the trigger decision. Immediately after the L1 trigger accept signal has been received by the on-detector electronics, the digitised information for the selected event is transmitted to the off-detector electronics. At the off-detector electronics, the Readout Drivers (RODs) accept digitised data from the on-detector electronics at a peak L1 trigger frequency of 100 kHz. The RODs are responsible for carrying out data processing activities in real time and for transmitting processed information in Level-2 (L2) trigger to the Readout Buffers (ROBs). To read 10000 channels, a maximum of 32 ROD modules are necessary [2].

1.1 Motivation

The LHC is currently undergoing the LS2 or Long Shutdown 2 in which the various experiments will maintain and replace their electronics. This will be followed by LS3 which will be used to upgrade for the HL-LHC. The HL-LHC aims to fully exploit the physics potential of the LHC by upgrading its current luminosity of 1×10^{34} cm^{-2}s^{-1} to 7.5×10^{34} cm^{-2}s^{-1}, corresponding to an average of 200 proton-proton simultaneous interactions per bunch crossing [3]. The increase in luminosity by nearly an order of magnitude above the original design would result in a corresponding increase in the detector particle flux and require a major upgrade in almost all ATLAS detector systems. Due to the number of collisions per bunch crossing, the calorimeter, inner tracker, trigger system and muon spec-

trometer of the ATLAS detector need to be upgraded to avoid the predicted degradation in the performance of the detector. To increase choice of events, the use of readout detector upgrades requires a new trigger architecture [3]. The TileCal was deployed more than 15 years ago using technology available at that time, the electronics are outdated and need to be upgraded. During the Test-Beam of the TileCal comprehensive beam tests are carried out with the final electronics designs of the planned HL-LHC TileCal upgrades. The results of these tests are discussed in this document in accordance with the planned physical output of the TileCal upgrade [3].

1.2 Overview of the Thesis

In Chapter 2 the overview of the Large Hadron Collider is given with the main focus being on the ATLAS detector and its different subsystems. Chapter 3 and 4 focus on the Tile Calorimeter and the overall online system of the ATLAS detector. Chapter 5 gives an overview of the TileCal upgrades in preparation for the HL-LHC. Chapter 6 gives a brief overview on the TileCal TB campaigns and the results from the electrons, muons and hadron beams.

Chapter 2

The ATLAS Detector of the LHC

2.1 The Large Hadron Collider

The LHC at CERN is the world's largest particle accelerator designed for a 14 TeV proton-proton center of mass and a design luminosity of F1 $\times$ 10^{34} cm^{-2} s^{-1}. It currently operates at a luminosity of 1 $\times$ 10^{34} cm^{-2} s^{-1} and a center of mass of 13 TeV. It consists of a huge superconducting magnet with a ring of length of 27 kilometers and a number of accelerating structures that boosts the number of particles along the way. The LHC was designed to discover new particles detecting the products of the interaction in proton-proton collisions. Inside the LHC, bunches of particles travelling in opposite directions with a speed close to that of light are made to collide [4]. The beam particles are directed around the LHC ring by the strong magnetic field sustained by the superconducting dipole [4]. In proton-proton collisions for a particular process, the number of events produced is obtained via equation 2.1 which depends on the physical process itself and the total integrated luminosity:

$$R = \sigma L, \tag{2.1}$$

where σ refers to the cross section of the process and L is the total integrated luminosity which is obtained by $\int L_{inst}dt$, while L_{inst} refers to the instantaneous luminosity. This quantity is obtained using equation 2.2, by measuring the beam parameters during specific LHC Runs called van der Meer (vdM) scans:

$$L_{inst} = \frac{1}{4\pi}\frac{N^2 f}{\sigma_x \sigma_y t}, \tag{2.2}$$

where N represents the number of protons per bunch, f represents the fraction of bunch positions containing protons, t is the time between bunches, and σ_x and σ_y are the transverse dimensions of the Gaussian beam profiles. All these parameters are configured in order to achieve a reasonable production rate for the physics process of interest [5].

The LHC (see Figure 2.1) consists of four major experiments: A Toroidal LHC Apparatus (ATLAS), Compact Muon Solenoid (CMS), A Large Ion Collider Experiment (ALICE) and LHC beauty (LHCb). The ATLAS and CMS experiments are multipurpose detectors that are designed for the discovery of new physics through proton-proton collisions. In 2012, after three years of operation, these two experiments announced a new elementary particle with a mass of 125 GeV, as predicted by the 50-year-old Brout-Englert-Higgs mechanism [6, 7]. The LHCb was designed to examine CP violation in the bottom-quark sector and ALICE is designed for quark-gluon plasma through heavy-ions, lead-lead and lead-proton collisions [8].

The upgrades, Long Shutdowns (LS) and Run periods define the activity stages of the LHC and its milestones. The upgrades refer to the LHC system and the modifications of the detectors that should be completed in 2021 and 2025. Respectively, the terms LS1, LS2, LS3 refer to the long shutdown periods of

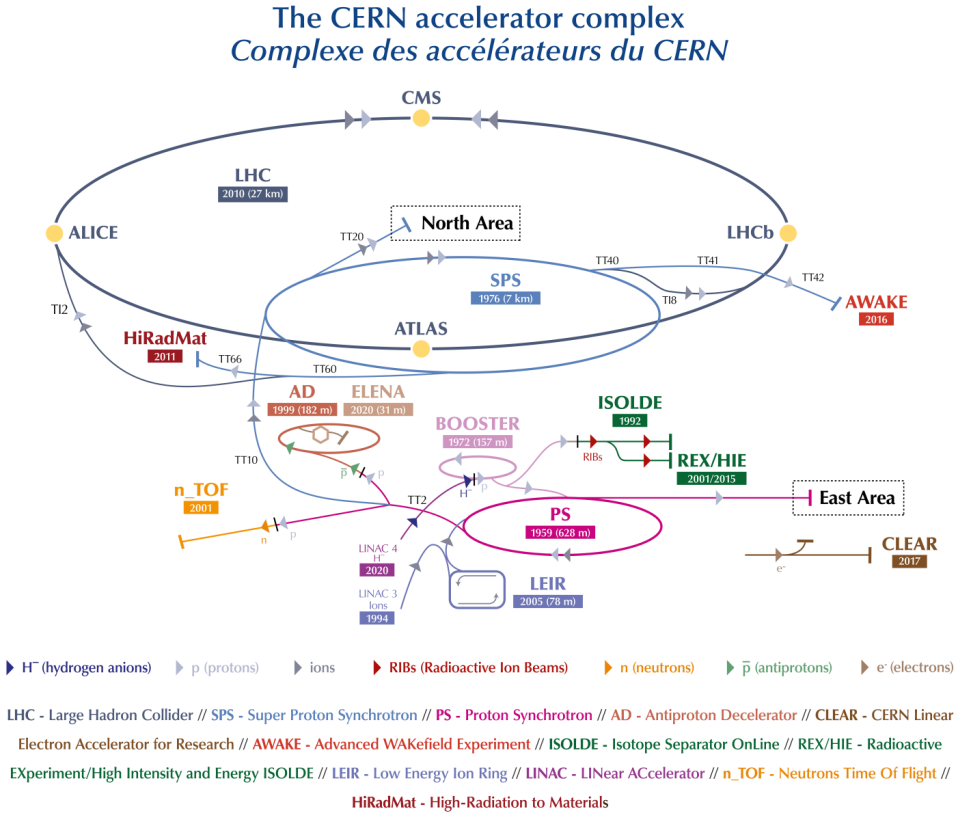


Figure 2.1: The LHC Accelerator ring displaying the different experiments [10].

the LHC machine during 2013-14 and are expected to be updated again in 2019, 2020 and 2024 until mid-2026. Run 1, 2 and 3 refer to the data acquisition period before and between the long shutdowns [9].

2.2 The ATLAS Detector

The ATLAS detector is one of the two multi-purpose experiments at the LHC and it is utilised for the search of new physics. The ATLAS detector has the shape of a cylinder; it weighs about 7000 tonnes with a length of 46 m and a diameter of 25 m. The detector consists of six different sub-detectors that are

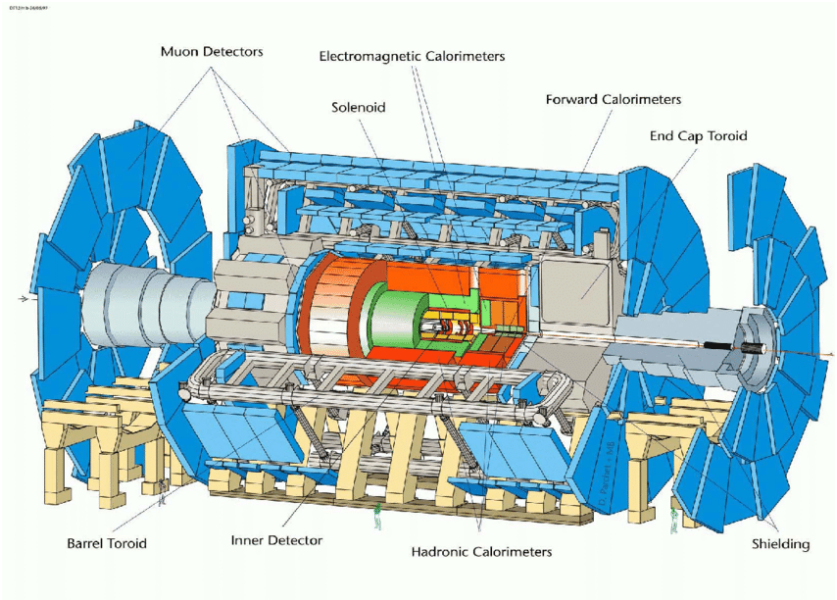


Figure 2.2: The ATLAS Detector and its components. The main components of ATLAS are the inner detector, the calorimeters, the muon spectrometer and magnet system and they are clearly displayed in this figure [13].

wrapped around each other in concentric circles around the collision point to record the momentum, energy and trajectory of particles. The different properties of the sub-detectors make it easy for the particles to be individually identified and measured, and there is a large magnet inside the detector that bends the paths of the charged particles to allow accurate measurement of the momenta of the particles [11, 12].

The ATLAS detector consists of four main components namely the Inner Detector (ID), Calorimeters, Muon spectrometer and a Magnet system. The ATLAS detector with its main components is shown in Figure 2.2.

2.3 Components of the ATLAS Detector

2.3.1 The Inner Detector

The Inner Detector (ID) in Figure 2.3 is contained within a cylindrical cover of length 7 m and a radius of 1.15 m, in a solenoid magnetic field of 2 T. The primary purpose of the ID is the high-precision measurement of the momentum and vertex resolutions, as well as the pattern recognition of charged particles tracks above a given transverse momentum p_T threshold and within a pseudo-rapidity of $|\eta| < 2.5$. It also provides electron identification and a wide range of energies in the range $|\eta| < 2.0$ [11, 14].

The ID consists of three main components: The Pixel Detector consisting of four pixel layers(IBL was added during LS0), Semiconductor Tracker (SCT) consisting of four layers of silicon micro-strip and Transition Radiation Tracker (TRT) a straw tube tracker split into 2 barrels and 2 end-caps. The pixel detector has the highest granularity and is situated nearest to the interaction point. The SCT is a silicon detector with micro-strips which surrounds the layers of the Pixel Detector. The pixel and SCT sub-detectors are commonly referred to as the Precision Tracker. The TRT resides in the larger radii, it constitutes many layers of gaseous straw-tubes elements interspersed with the transition radiation material. The TRT provides continuous tracking with an average of 36 hits per track thus providing continuous tracking to enhance the pattern recognition and improve the momentum resolution over $|\eta| < 2.0$ and electron identification compatible to that of the calorimeter over a wide range of energies [12, 15]. Figure 2.3 displays the ATLAS ID with its sub-systems.

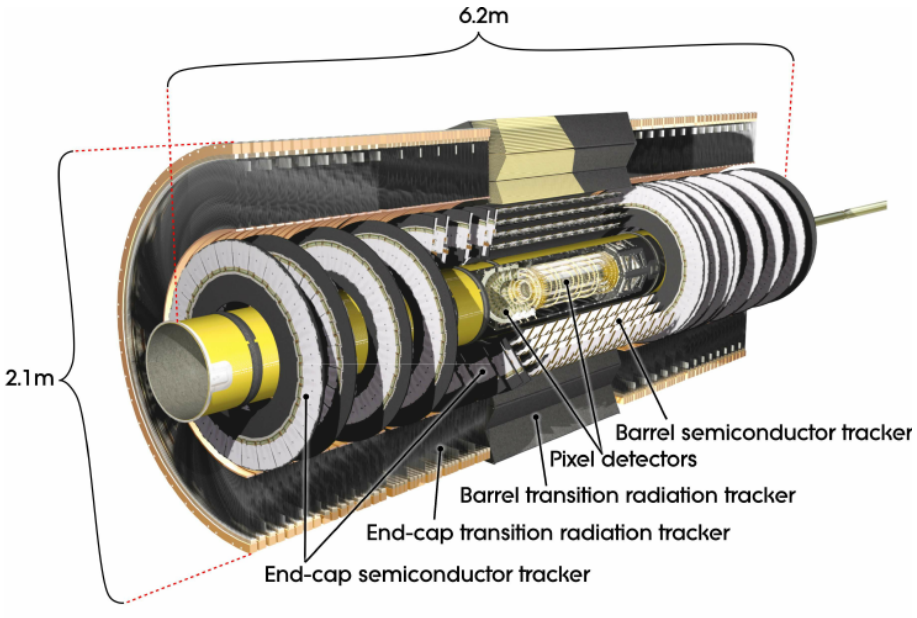


Figure 2.3: The ATLAS Inner Detector [5].

2.3.1.1 The Pixel Detector

The pixel detector resides in the inner-most layer of the inner detector and it consists of four barrels with an average radii of approximately 3 cm, 4 cm, 11 cm and 14 cm and three disks on each side between radii 11 cm and 20 cm completing the angular coverage. Its sole purpose is the high-granularity and high-precision measurements closest to the interaction point. It provides three of the precision measurements over the full acceptance, and determines the impact parameter resolution and the ability of the ID to find short-lived particles such as b-quarks and τ-leptons [14, 15].

The pixel detector system contains a large amount of modules with an approximate number of 1500 identical barrel modules and 1000 identical disk modules and uses only type of support structure in each of the types of modules. The modules are similar in terms of design for the disks and barrels. Each barrel

modules has the dimensions of 62.4 mm length and 22.4 mm width, with 61440 pixel elements read out by 16 chips each serving an array of 24 by 160 pixels, for the 3 outer pixel layers, and 20×20 mm^2 modules, with 26880 pixels of size 250×50 m^2 in the first layer (IBL). The chips must be able to withstand radiation, as they will be exposed to ionising radiation of 300 kGy and over a NIEL of 5×10^{14} 1 MeV neutron equivalent per cm^2 in ten years of operation. The detector offers about 140 million pixels, with position measurements of 50 μm in the Rϕ direction and 300 μm in the z-direction [12, 15].

2.3.1.2 The Semi-Conductor Tracker

The Semi-Conductor Tracker (SCT) is designed to provide four precision measurements per track in the middle layer of the ID. This contributes towards the momentum, impact parameter and vertex position measurements, as well as the high granularity pattern recognition. It uses four layers of silicon micro-strip detectors with each detector being 6.36×6.40 cm^2 with 768 readout strips each with a pitch of 80 μm. The four detectors provide precision points in the $R\phi$ and z-directions, making use of a small angle stereo to obtain the z measurement [16]. The barrel modules are mounted on local supports which only allows a maximum of six units of modules to be tested together before being mounted on the carbon-fiber cylinders which carry cooling system, the four complete barrels at radii of 300 mm, 373 mm, 447 mm and 520 mm are then linked together [14, 15].

2.3.1.3 The Transition Radiation Tracker

The Transition Radiation Tracker (TRT) resides on the outer layer and is based on the use of straw detectors. Each straw has a diameter of 4 mm, this gives it a fast response and a mechanical properties for a straw as long as 150 cm. The straws can function at the very high rates needed by virtue of their small diameter

and the isolation of the sense wires within individual gas envelopes [16]. The TRT provides good pattern recognition by continuous tracking (approximately 36 hits per track) and it contributes to the electron identification, which is possible by the employment of xenon gas utilised for the detection of the transition-radiation photons that is produced in a radiator between the straws [14, 15].

2.3.2 The Calorimeters

The ATLAS calorimeter (see Figure 2.4) consists of the Electromagnetic Calorimeters (ECAL) and Hadronic Calorimeters (HCAL). They cover the pseudo-rapidity region of up to $|\eta| < 4.9$. The calorimeters measure the energy of the showers of charged and neutral particles resulting from proton-proton collisions in the LHC. The ECAL measures photons and electrons and the HCAL measures the hadrons, as well as the charged and neutral particles. The calorimeters differ in terms of technology: the ECAL is based on the Liquid Argon (LAr) technology and the HCAL is based on the scintillating tiles technology [12, 15].

2.3.2.1 Electromagnetic Calorimeters

The Electromagnetic Calorimeter (ECAL) surrounds the ID, it is a sampling detector with accordion-shaped electrodes that uses Liquid Argon (LAR) as the active material, and lead as an absorber. It consists of three longitudinal layers split into one barrel (EMB) covering the pseudo-rapidity region of $|\eta| < 1.475$ and two end-cap barrels (EMEC) covering the regions $1.375 < |\eta| < 3.2$. An additional pre-sampler is installed in in the barrel region that covers the pseudo-rapidity $|\eta| < 1.52$ and the pre-sampler in the end-cap region covers $1.5 < |\eta| < 1.8$. It has a thickness of $X_0 > 22$ radiation lengths in the barrel region and $X_0 > 24$ in the end-cap region [12, 15]. Figure 2.5 displays a cut-way view of the ECAL, plus other LAR based hadronic calorimeters explained in the next

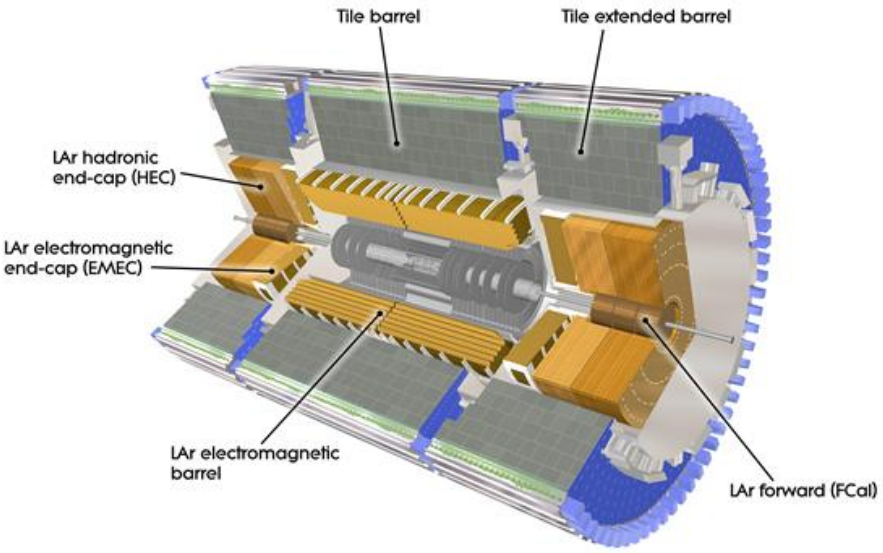


Figure 2.4: Cut-away view of the ATLAS calorimeter. The LAR calorimeters are shown inside the scintillator [17].

section.

2.3.2.2 The Hadronic Calorimeters

The The Hadronic Calorimeter (HCAL) system is divided in terms of pseudo-rapidity coverage: in the central region $|\eta| < 1.7$ the HCAL is a plastic scintillating calorimeter (TileCal); in the forward region $1.5 < |\eta| < 3.2$ HCAL is a hadronic end-cap calorimeter (HEC) and in the region $3.1 < |\eta| < 4.9$ it is a Forward Hadronic Calorimeter (FCAL). The TileCal is situated behind the ECAL and the solenoid magnet. It is a sampling calorimeter that uses steel as an absorber and scintillating tiles as an active medium. It is divided into a central Long barrel (LB) in the region $|\eta| < 0.8$ and two extended barrels (EB) in the region $0.8 < |\eta| < 1.7$. Each barrel consists of 64 azimuthally segmented modules. The TileCal has an inner radius of 2.28 m and an outer radius of 4.25 m. The LBs and EBs are segmented in depth in three layers (A, BC, D) having the thickness

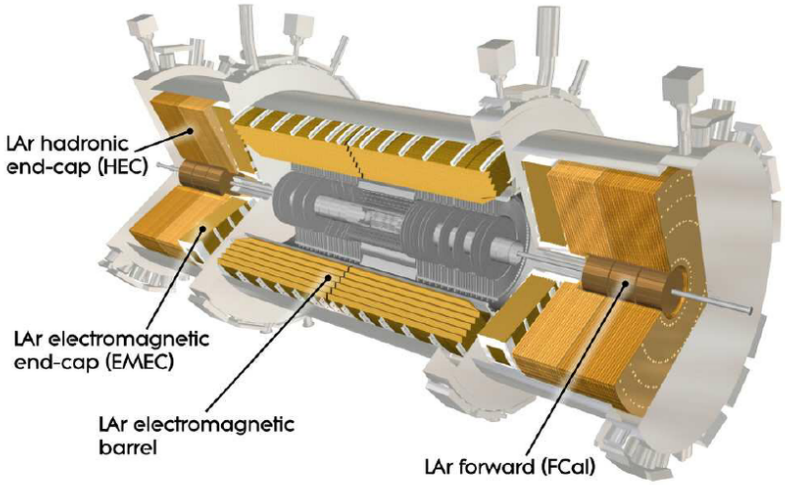


Figure 2.5: A remote view of the calorimeters that use LAR as active material [18].

of approximately 1.5, 4.1 and 1.8 interaction lengths (λ) in the LB and the EB having approximately 1.5 λ, 2.6 λ and 3.3 λ. Figure 2.6 displays the segmentation and the optical readout of the TileCal, in which the optical output of the tiles is grouped into cells with segmentation $\Delta\eta \times \Delta\phi$ is 0.1 $\times$ 0.1 for A and BC type cells and 0.2$\times$0.1 for D type cells as shown in Figure 2.7.

The The Hadronic EndCap (HEC) is a copper/liquid argon sampling calorimeter with a flat-plate design and it covers the end-cap range $1.5 < |\eta| < 3.2$, that is located inside the end-cap cryostats. The HEC consists of two wheels at each side of the interaction point: a front-wheel (HEC1) and a rear-wheel (HEC2), with two longitudinal sections for each wheel. The wheels are cylindrical with an outer radius of 2030 mm. Each HEC wheel comprises 32 identical modules with the same wedge shape. The front wheel modules consist of 24 copper plates with a thickness of 25 mm each, plus a 12.5 mm thick front plate. The sampling fraction

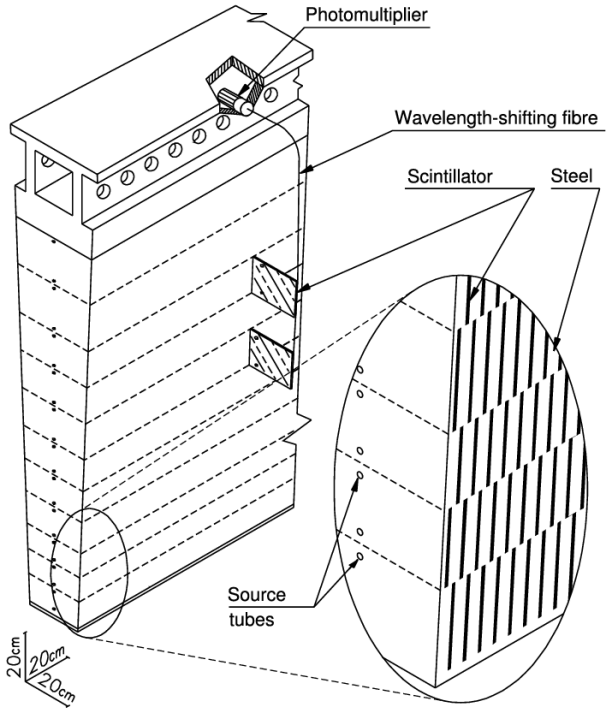


Figure 2.6: Schematic displaying the mechanical structure and the optical read-out, corresponding to a Φ wedge of the TileCal so called module [19]. There are 11 rows of tiles in the radial direction.

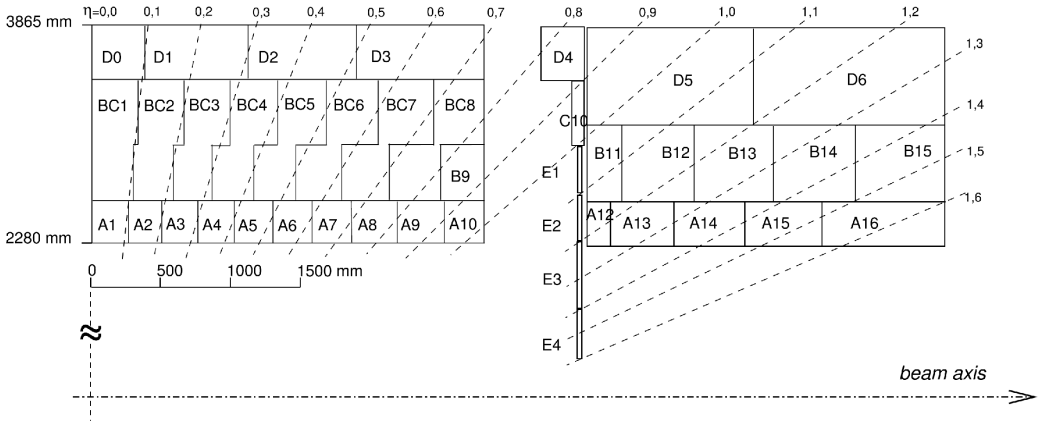


Figure 2.7: Schematic of the TileCal distribution for half of a long module barrel (left) and an extended module barrel (right) with lines showing the projective pseudo-rapidity distribution [19].

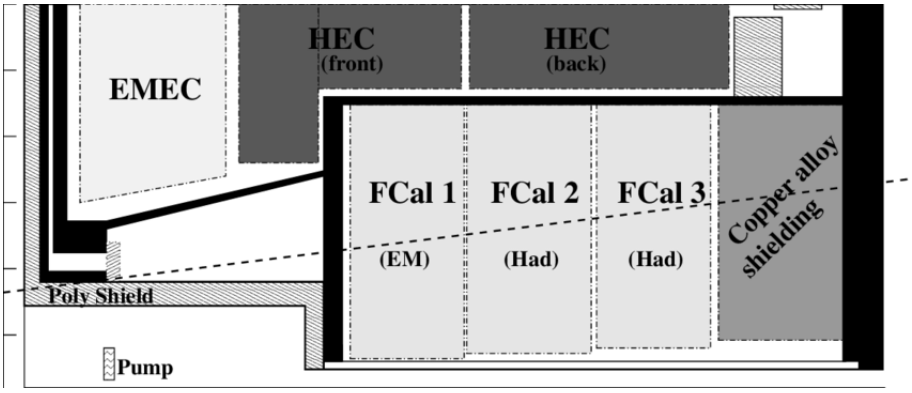


Figure 2.8: A schematic diagram showing the three modules of the FCAL located in the cryostat end of the heading [20].

in the rear wheels is more rough, with 16 copper plates each 50 mm thick, and the front plates are 25 mm thick. The spacing between the plates is 8.5 mm thick [12].

2.3.2.3 The Forward Calorimeters

The The Forward Calorimeter (FCAL) positioned within the same cryostats as the HEC, covering the region $3.1 < |\eta| < 4.9$. Every FCAL is divided into three 45 cm deep modules: one electromagnetic (FCAL1) modules and two hadronic (FCAL2 and FCAL3) modules. Copper was chosen for FCAL1 as the absorber for optimum heat removal and resolution, while tungsten was primarily used in FCAL2 and FCAL3 to preserve and mitigate the lateral dispersion of hadronic showers. A copper alloy shielding plug was installed behind the FCAL3 to decrease the background of the end-cap muon system. The FCAL1 layer consists of copper plates that are stacked behind one another and there are 12,260 holes in the plates, through which the electrodes are mounted. An electrode is made up of a copper rod and a copper tube separated from each other by a precision, plastic radiation hard fiber. The mechanical integrity can be achieved by making use of a set of four tie-rods that are bolted through the structure. The electrode

pipes are swaged to provide a good electrical connection at the end of the signal [12]. Figure 2.8 displays how the FCAL modules are aligned. The shielding plug behind the material in front of FCAL is also shown. The black regions are structural components of the cryostat. The diagram is visually wider in order to make it simpler.

2.3.3 The Muon Spectrometer

The muon spectrometer (see Figure 2.9) surrounds the calorimetry system. The main purpose of the muon spectrometer is to detect and measure the momenta of the muons leaving the barrel and the end-cap calorimeters in the pseudo-rapidity range of $|\eta| < 2.7$. The muon spectrometer achieves the full measurement of the muon momenta with the three stations of precision tracking chambers located on and between the eight coils of the superconducting barrel toroid magnet in the barrel region, while in the two end-cap regions it resides both at the front and behind the two end-cap toroid magnets [12, 15].

In the barrel region the muon chambers are arranged in three concentric cylindrical shells of the detector with radii of approximately 5 m, 7.5 m and 10 m. Respectively, in the end-cap regions the chambers form large wheels that are aligned perpendicular to the z-axis and are located at distances $|z| \approx 7.4$ m, 10.8 m, 14 m, 21.5 m.

The Monitored Drift Tubes (MDT) chambers, which cover the range $|\eta| < 2.7$ (except in the innermost end-cap layer where their range is limited to $|\eta| < 2.0$) performs the measurement of accuracy through a combination of high precision calculation, predictability of mechanical deformations and simplicity of design. The MDTs are aluminium tubes with a diameter of 30 mm, and 400 μm thick-

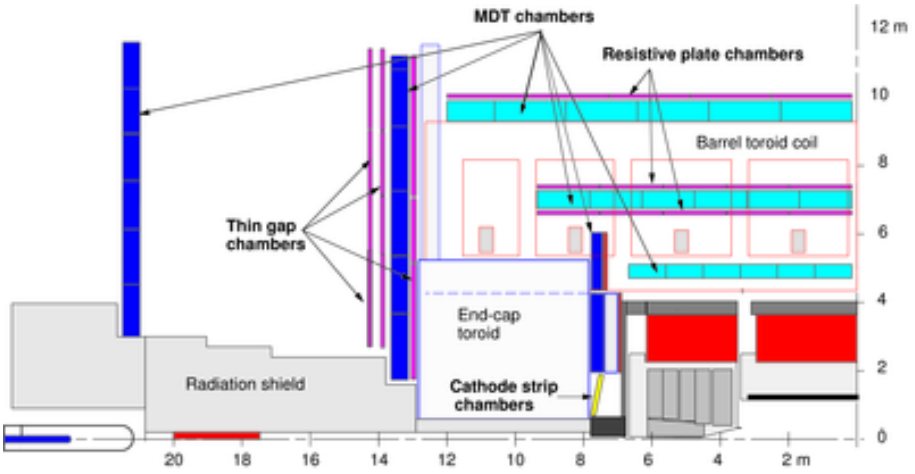


Figure 2.9: The ATLAS Muon Spectrometer [21].

ness with a 50 μm diameter of Tungsten-Rhenium wire. Each MDT is coupled to an Resistive Plate Chamber (RPC) that is a faster muon detector that provides information to the L1 trigger system [12, 15].

The Cathode-Strip Chambers (CSCs) covering the range $2.0 < |\eta| < 2.7$ are utilised in the innermost layer due to their higher rate capability and time resolution. The CSCs are multi-wire proportional chambers with cathode strip readout and in orthogonal symmetry [12, 14]. The Thin Gap Chambers (TGC) are located in the forward region of ATLAS, it is divided into 3 wheels on each side, with up to 6 different types of modules, and provides a trigger coverage from $1.0 < |\eta| < 2.7$.

2.3.4 The Magnet System

The ATLAS magnet system is a system of superconducting magnets arranged in optimised positions around the collision point. The four superconducting magnets are the central solenoid, which provides the magnetic field for the inner detector, the eight air-core superconducting magnets for the barrel toroid and two end-cap

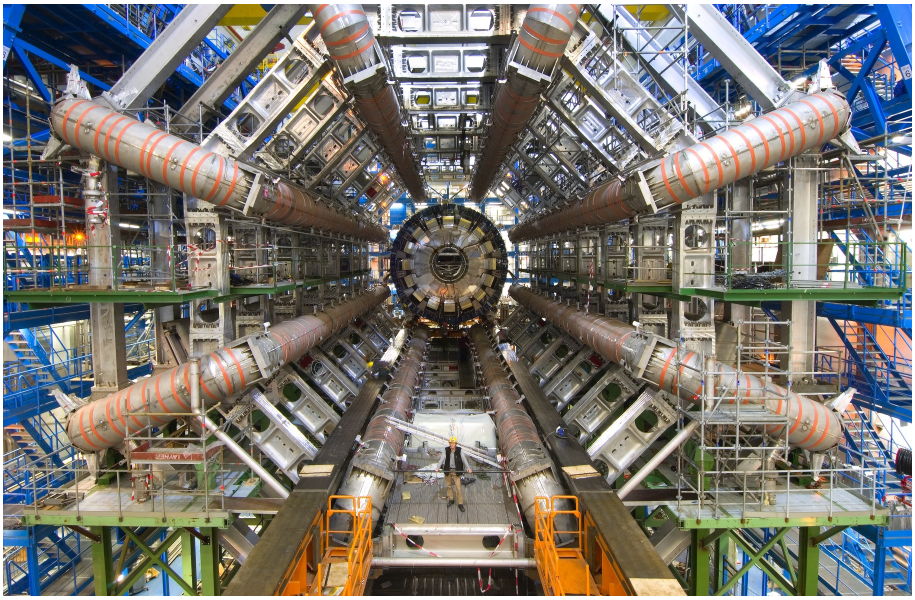


Figure 2.10: The Magnet System of the ATLAS detector [22].

toroids that provides the toroidal field configuration for the muon spectrometer. The dimensions of the system are driven by the size of the barrel toroid which has a 26 m diameter, 20 m length and a volume of 8000 m^3. The two end-cap toroids reside on each end of the barrel toroid and are lined up with the central solenoid. They are 5 m long with inner and outer diameters of 1.65 m and 10.7 m. The central solenoid is about 5.3 m long with a diameter of 2.4 m. The solenoid is hosted inside the cryostat of the ECAL [12, 15].

The central solenoid provides a magnetic field of 2 T with a magnetic field peak of about 2.6 T on the superconductor in the windings. The magnetic field peak in the barrel and end-cap toroids is about 3.9 T and 4.1 T. Each of toroids consists of eight coils that are placed in separate cryostats. Respectively, the end-cap coils are rotated 22.5° with respect to the barrel coils in order to provide radial overlap and to optimise the bending power in the interface regions of both coil systems. Figure 2.10 shows the magnet system of the ATLAS detector.

2.4 The ATLAS Trigger and Data Acquisition Systems

The proton-proton collisions at the LHC generate a huge amount of data. However, not all the data have characteristics that are deemed useful. The ATLAS detector uses a specialised three-level online trigger system that reduces the amount of data to manageable levels. The ATLAS Trigger system is a system that analyses and selects events that have characteristics that makes them seem interesting for physics analysis. The trigger system consists of three distinct levels Level-1 (L1), Level-2 (L2) and the Event Filter (EF). The L1 trigger is implemented using custom-made electronics, the L2 and the EF trigger forms the High-Level trigger (HLT) and they are based on commercially available computers and network hardware [12, 23, 24].

The Data Acquisition (DAQ) system is designed to handle the data from the detector at the L1 trigger rate. The data transmission from the detector is done through point-to-point Readout-Links (ROLs). The data requested by the trigger is transmitted from the L1 to the L2 through ROLs, event-building is performed for the events fulfilling the L2 selection criteria. The selected events in the L2 are then moved by the DAQ system to the EF and the events selected there are then moved to permanent event storage. The DAQ system is also in charge of the configuration, control and monitoring the ATLAS detector during data-taking period [12, 25]. Figure 2.11 displays the overview of the TDAQ system during the 2015-2018 data-taking period.

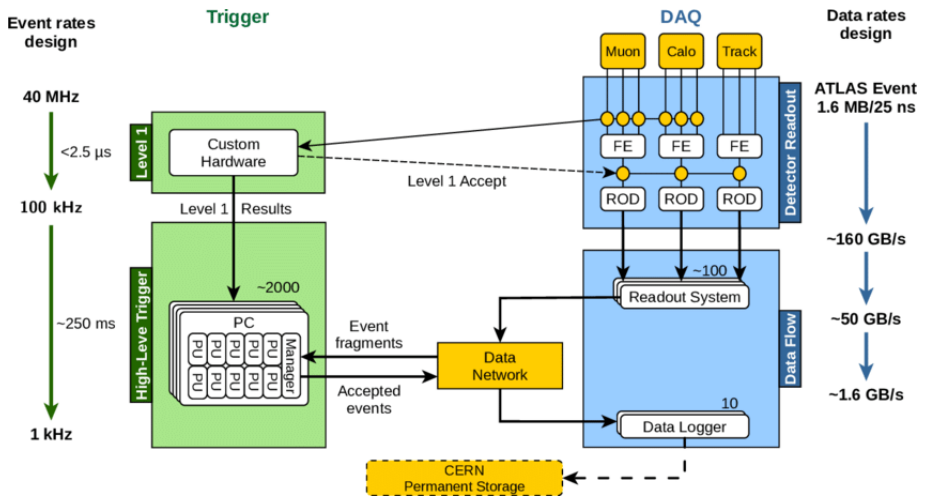


Figure 2.11: ATLAS Trigger and Data Acquisition System Outline, showing an occurrence and data levels expected for the data acquisition during the 2015-18 data-taking period [26].

2.4.1 The Level-1 Trigger

The L1 trigger is based on the custom made on-detector electronics. The initial event-selection is performed at the L1 trigger, the events selected are based on the information received from the calorimeters (information is received from all the calorimeters i.e ECAL, TileCal, HCAL and FCAL) and muon detectors. The purpose of the L1 calorimeter trigger is to identify high p_T electrons, photons, jets, τ-leptons that decays into hadrons with a high energy in the transverse plane. It also selects events with large missing transverse energy (E_T^{miss}) and large total transverse energy. Isolation may be required for the high energy particles identified. Isolation suggest that the energetic particle in the same trigger must have a minimum angular separation from any significant energy deposit [12, 27].

The L1 muon trigger identifies all the signals in the muon trigger chamber: RPCs in the barrel region and TGCs in the end-cap region. The trigger studies and identifies patterns of hits similar with the high momentum muons originating

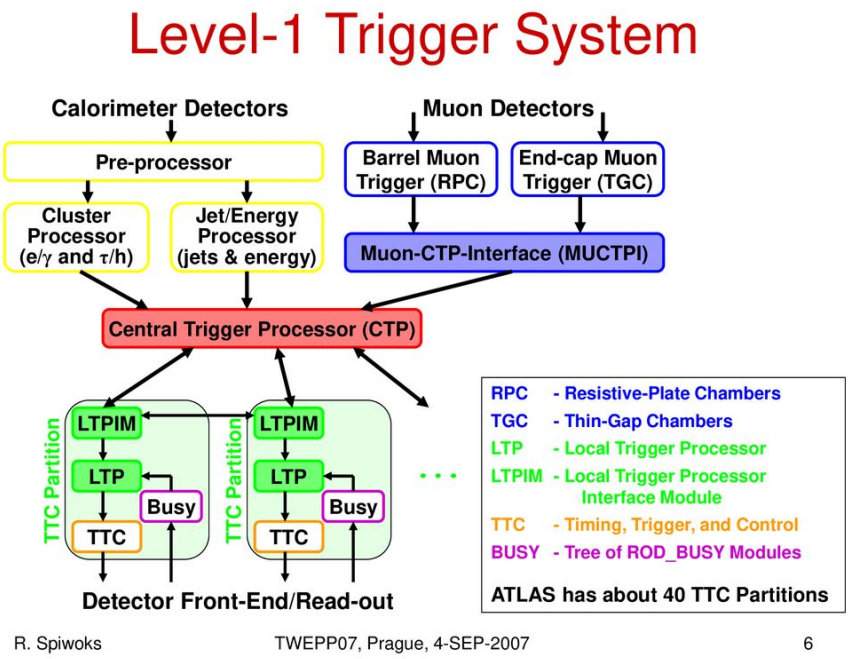


Figure 2.12: The architecture of the L1 trigger system [28].

from the interaction point.

The Central Trigger Processor (CTP) oversees the overall accept decision of the L1 trigger and it combines the information for the different object types. The trigger menus can be programmed with up to 256 distinct items, with each item being a combination of the required input data. Figure 2.12 shows the architecture of the L1 trigger system. The calorimeter analog data is digitised and linked to the correct bunch crossing in the pre-processor and then sent to the Jet/energy-sum processor and the cluster processor, two algorithmic processors [12, 28].

2.4.2 The High-Level Trigger

During the L1 trigger event selection, the event data is buffered in memories that reside in specific Front-End (FE) electronics. The selected data is transferred to the HLT over 1574 Readout Links (ROLs). The 1574 event fragments are obtained by the 1574 Readout Buffers (ROBs), which are accommodated by the Readout System (ROS) which stores them for a limited period before being provided on request to the subsequent stages of the HLT/DAQ system [12]. The L1 trigger subsystems (calorimeter, muon and CTP) also provide the Region of Interest (ROI) data on eight ROLs, a dedicated data line, for every selected event to the ROI builder, where it is assembled in a single data structure, and transmitted to one L2 supervisor (L2SV). The activities in the L2 signal are marshalled by the L2SV. It gets the ROI, assigns each event for the analysis to one of the L2 trigger units (L2PUs) and receives the results of the analysis from the L2PU. Requests for event data are made to the corresponding ROS using the ROI information [24].

The HLT farm in Run 2 does not distinguish between L2 and EF nodes. Both algorithms are run on the same node. Each node implements a Data Collection Manager (DCM), that receives the ROI from the ROIB and decides if it will request data from the ROS or not. The data is only transferred out of the ROS once, reducing the data bandwidth usage. The DCM reports back to the ROIB that it finished processing the event.

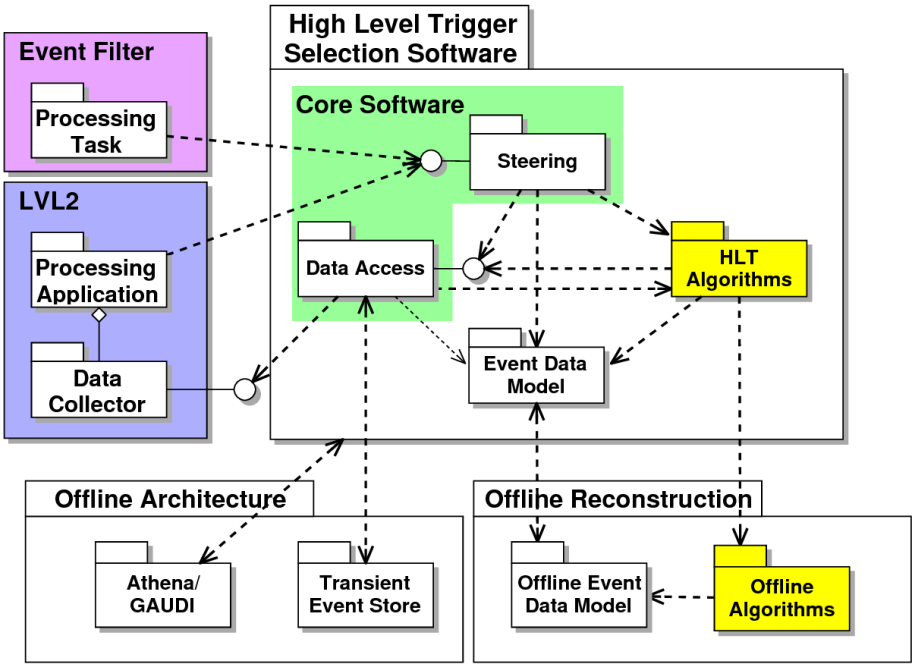


Figure 2.13: Overview of the ATLAS High Level Trigger selection software [29].

Chapter 3

The Tile Calorimeter

The TileCal is a sampling calorimeter that reside in the innermost part of the ATLAS detector and is used to measure energies carried by charged and neutral particles. It consists of two EBs and one LB. The TileCal is split into four partitions such as EBA and EBC for the EB and LBA and LBC for the LB. Each partition consists of 64 azimuthally-segmented modules that are mounted with the super-drawers. The super-drawers are embedded with a number of electronics that have different roles in the functioning of the TileCal [25].

Each module contains a matrix of steel plates with tiles of plastic scintillators sandwiched in between. The scintillating tiles are grouped into cells (A, BC and D), as shown in Figure 2.7. The cells are readout on both sides by the Wavelength Shifting fibers (WLS). The WLS are in turn read-out by the Photo-Multiplier Tubes (PMTs) located along with the rest of the (FE) electronics in the super-drawers axially oriented at the maximal radius of the barrels. The FE electronics are powered by the Low-Voltage Power Supplies (LVPS) which resides at the outer radius of the module and is controlled from the Detector Control System (DCS). The electronics are protected from radiation by the calorimeter steel

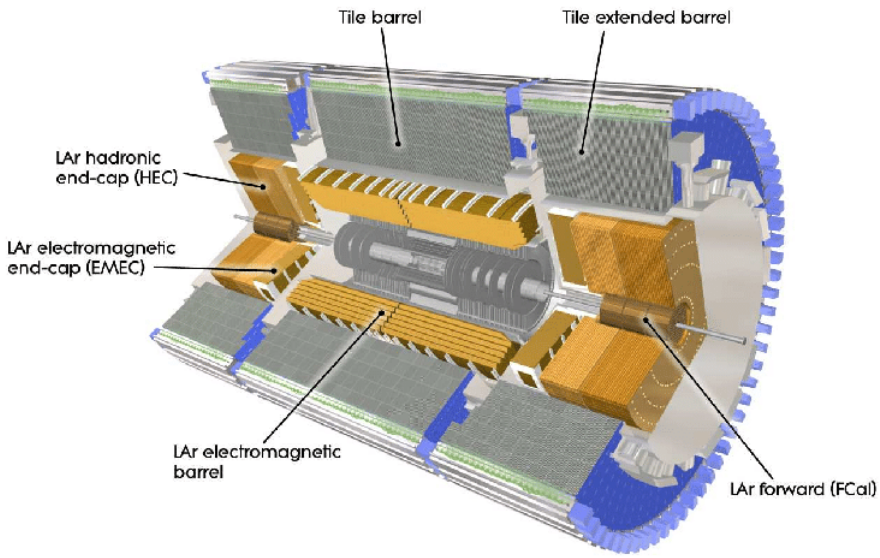


Figure 3.1: The ATLAS Calorimetry system [17].

plates. The FE electronics are those housed inside the super-drawer: Motherboard, Interface board, Digitiser board, Adder board, High-Voltage (HV) board , 3-in-1 cards and PMTs. The FE electronics have important functions such as summing up the PMT signals originating from different cells to form a fast analog trigger signal [30].

The data from the FE electronics is transferred to the Back-End (BE) electronics for further processing and readout to permanent storage. The communication between the FE and BE electronics is done through redundant optical links, which are of two types: write only which are used for the Timing, Trigger and Control (TTC), and the read only which are used for Readout. Finally, the TileCal is instrumented with three detector calibration systems namely the Charge Injection System (CIS), the Laser system and a Cesium (^{137}Cs) radioactive system. Together, these systems are used to maintain the calibration of TileCal to the electromagnetic scale with a very good precision [25]. The calibration factor was

extracted from the test-beam campaign in 2005.

3.1 The TileCal Front-End Electronics System

The FE electronics are the on-detector electronics that are housed inside the super-drawer. Each super-drawer consists of two electronically connected drawers and can be inserted easily inside the module girders. The TileCal consists of two extended barrels (EBA, EBC) with 64-modules each, and one long barrel instrumented from both sides with 64 modules (LBA, LBC). A total of 256 super-drawers constitute the front-end electronics of the TileCal. The super-drawer consists of a number of different electronics with each electronic playing a different role. The electronics inside the super-drawer are listed and explained below [25]. Only 45 PMTs are instrumented in the LB super-drawers, and 32 in the EB super-drawers.

3.1.1 The Mother-board

The basic element that holds all the other electronics inside a super-drawer. Two mother-boards are placed in every super-drawer. It gives power and TTC commands to the 3-in-1 card. 4 digitiser boards and one interface board are hosted on the mother-board [25, 31].

3.1.2 The Interface Board

The interface board is placed in the middle of the super-drawer and receives the digitised signals from the Data Management Units (DMUs) and distributes TTC signals to the rest components inside the super-drawer. It realigns the data to a common clock and packs them together into 32-bit words and transmits the data through optical links to the BE electronics [15] together with Cyclic Redundancy

Checks (CRC) that are performed on the input and output data streams. The memory in the interface board holds up to 16 event frames containing 7 samples of 10 bits for each PMT [31].

3.1.3 The Digitiser-Board

The digitiser boards are connected to 6 PMTs. The digitiser receives the high and low signals from the 3-in-1 cards inside the PMTs. The signals are digitised every 25 ns by the 10-bit ADCs which utilises the TTC clock system that can be adjusted in 106 ps units. Each digitiser board consists of two DMUs, which are custom ASIC chips which store data temporarily in pipeline memories awaiting L1 Accept (L1A). One DMU can process digitised samples from three PMTs, thus 2 DMUs are mounted on each digitiser board. The digitiser board is also equipped with the TTC receiver (TTCrx) [25] chip which is responsible for the timing and programming of the digitiser system. There are 8 digitiser boards in the LB super-drawer which reads out 45 PMTs and 6 digitiser boards which reads out 32 PMTs in the EB super-drawer [25, 31]. Figure 3.2 displays the block diagram for the digitiser system.

3.1.4 Photo-Multiplier Tube Block

The PMT block (see Figure 3.3) is a compact instrument that converts the light signal to analog signal. Each super-drawer can house up to 48 PMTs. It contains the 3-in-1 card, light mixer, HV Divider and a PMT. The PMT blocks are located on the outer radius of each module. The light mixer is placed between fiber bundle and the photo-cathode and mixes the light originating from the fibers. The location of the mixer ensures that there is no correlation between the position of the fiber and an area around the photo-cathode which receives light.

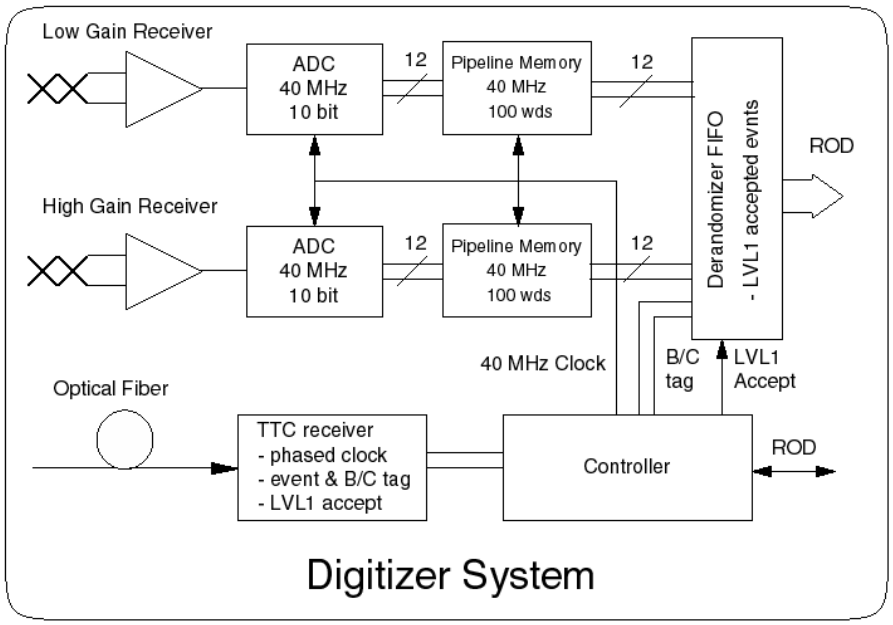


Figure 3.2: The block diagram for the digitiser system [25].

The PMT is responsible for the measurement of light originating from the scintillators. The PMT employed at the TileCal is a Hamamatsu R7877 (special evolution of the R5900 model) which is very compact with a dinode structure of about 8 – 10 amplification stages.

The HV divider is a printed circuit board with surface mounted components and is attached to the 3-in-1 cards. Two additional HV bus cards and two HV opto-controller cards installed in the super-drawer are able to provide individually tuned HV to the 24 PMTs. The HV distribution is controlled by an HV micro connected to the ELMB card for the slow control of the super-drawer.

The 3-in-1 card is a printed circuit board with dimensions of 7 cm $\times$ 4.7 cm. It is responsible for most of the analog functions of the electronics inside the drawer. The PMT pulse produces a standard signal shape for all the channels by the

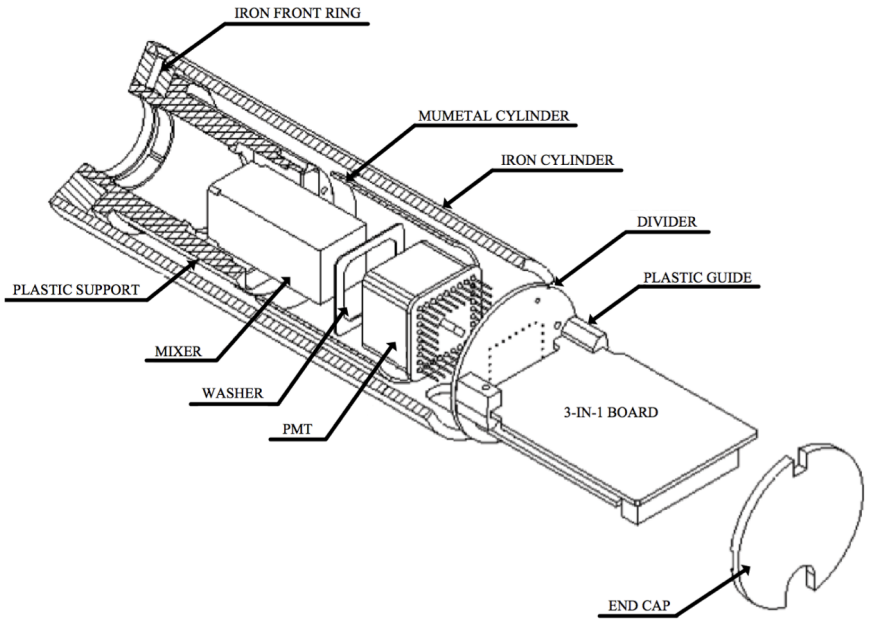


Figure 3.3: Schematic of a PMT Block [25].

removing the pulse by pulse fluctuation in the raw signal. The standard signal in amplified to produce two signals with a ratio of 1:64, corresponding the low and high gain range. It provides the (CIS) system which allows for the injection of a known charge into the input of the signal shaper and slow integrator amplifier which is used for the cell calibration and monitoring [31].

3.1.5 Adder Boards

The adder boards are mounted on the mother-board. Each adder board receives the analog trigger output signals from a maximum of 6 3-in-1 cards, the inputs are combined to form analog trigger signals. The input signals are summed up by the adder and two readout signals are sent out through the long cables to the L1 trigger system. From the two output signals, one contains the summation of all samples and the other signal is the summation of the muon samples [25].

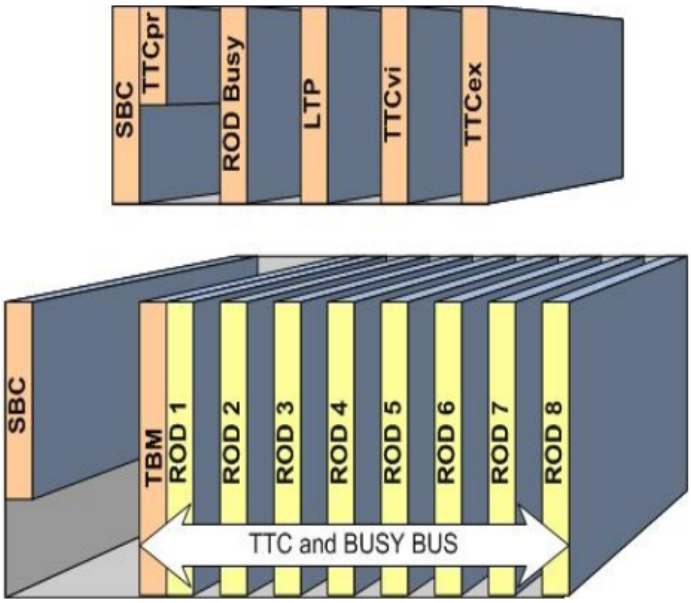


Figure 3.4: The TileCal Back-End electronics partitions [30].

3.2 The TileCal Back-End Electronics System

The BE electronics system for the TileCal is organized in four partitions (see Figure 3.4), with two of the partitions servicing the LB and the other two servicing the EB. Each of four partitions consists of its own TTC and Readout Units. Each partition is divided into a 6U Versa Module Euro-card (VME) TTC crate and 9U VME ROD, which readout all the 64 super-drawer modules in all the barrels [12, 25]. The back-end system of all the calorimeters is located at the main services cavern (USA15), which resides 70 m away from the ATLAS detector. The TTC and ROD crates are controlled by the Single Board Computer (SBC) 6U VME module [12, 25].

The crates are also monitored and powered by the DCS. The VME modules are described in the following sections.

3.2.1 Trigger Timing and Control Module Crates

The TTC system is implemented by the utilisation of four VME crates, where each single crate implements up to two partitions. Each single crate contains a controller and a Local Trigger Processor (LTP). The purpose of the LTP of the ATLAS detector is to receive the TTC signals from the CTP and inject them into TTC system of the sub-detector. The Local Trigger Processor Interface (LTPI) VME module that interfaces multiple LTP modules with the CTP and it also allows communication between sub-detectors. The ATLAS TTC VME bus interface (TTCvi) is in charge of the interaction between the local TTC system and the global TTC system. The ATLAS TTC emitter (TTCex) [25] is a laser transmitter module, it converts commands from the TTCvi into the optical signals that are further transmitted to the FE electronics. The busy module of ATLAS ROD tracks the busy, calculates it in bunch crossing units, and generates the sum of each of its 16 busy input lines that can be conveniently masked [25].

3.2.2 Shaft Module, TTC Receiver in PMC Form Factor, Trigger and ROD busy

Shaft module is a 6U VME module that controls the various requests for the TileCal calibration trigger. The TTC PMC Form Factor Receiver (TTCpr) is a specific TileCal card that is plugged into the SBC. Its main function is to provide the event identification, bunch crossing identification and trigger type for each event recorded in the data. The Trigger and Busy module is a 9U VME module for the ROD crate module. It receives TTC signals from the optical link of the local TTC system [25].

3.2.3 Laser Readout Driver and Readout Driver

The Laser ROD is a 6U VME module that provides information from the laser calibration system to the data-flow and provides TTC signals to the Laser System. The ROD driver is a 9U VME module that receives data from the 8 FE links of the super-drawers [25]. There are 8 ROD modules per partition, each one reading out 8 super-drawers.

3.3 The Calibration Systems

The TileCal calibration system is divided into three sections: the optical part that consists of fibers and scintillators, the PMTs, the FE part that digitises and shapes the light signals. Each of these sections is independently accredited by the calibration and monitoring system.

3.3.1 The Charge Injection System

The Charge Injection System (CIS) system has been designed to correctly calibrate the FE shaping and digitising circuits by 1%. Every TileCal PMT channel is bi-gain (consists of two analogue paths), the high and low gains are 82 counts/pC and 1.3 counts/pC, is digitised by a 10 bit ADC and covers an 800 pC range. The CIS constants allow ADC counts to be converted to energy. Each channel has calibration capacitors that are charged and released to the input electronics from an extremely precise voltage source. The CIS runs are taken, which scans the full range of charges for both gains and allow each channel to determine the number of ADCs/pC. The amplitude of the pulses is reconstructed with a 3 parameter fit from ADC samples every 25 ns [32, 33].

3.3.2 The Laser System

The laser system was intended to calibrate and accurately monitor the PMT response by more than 0.5%. It will be used for monitoring PMT linearity, for pulse saturation and calorimeter timing studies as well as for debugging and diagnostic testing. A Nd:YVO4 double frequency laser is used to produce pulses that are synchronised with a wavelength of 532 nm and a width of a $\sim$10 ns. In close proximity to the laser, the LED is shared by sending part of it to a set of photo-diodes for monitoring relative intensity, and the rest to each PMT calorimeter via a light distribution system and transparent optical fibers. The most important role of the system is to monitor PMT gains in the short and long term. This is achieved in the special calibration ranges from the charge ratio of each PMT to the photo-diode response of the laser pulse. The relative gain of each PMT is given by this ratio. The results from the TB conditions show the reliability of PMTs and the accuracy of the laser system match the design target. In a known range, the linearity of PMTs may differ in the intensity of the light provided. While the laser intensity itself can only be varied by a factor of 10, an automatic collection of filters enables an additional dynamic range of more than 1000. In combination with the measured calorimeter response in pC/GeV the laser system is also used to measure the absolute gain of all PMTs and the photo-electron output may be obtained. It benefits from the precise tracking of the pulse-to-pulse intensity fluctuations at the laser with the photo-diodes monitored. In timing studies, the laser system is also useful because the differences in signal spreading can easily be correlated with projection particle and laser pulses. High-intensity laser pulses can be transmitted to PMTs in order to saturate the reading response and then use saturation recovery strategies [32, 33].

3.3.3 Cesium System

The Cesium (Cs) calibration is designed to determine the performance of the optical reactions of each calorimeter cell, adjust the HV of the PMT to equalize and monitor the response of all cells over time. The goal of Cs calibration is to maintain the energy calibration stability at 0.5%. The system use ^{137}Cs γ source that move through a hole in the scintillating tiles, orthogonal to the them. This source is transported through a hydraulic system in a number of direct paths along the calorimeter modules and passed through the holes in each tile and absorber base. The current of each PMT is measured using an integrator that samples the signal at a rate of 90 Hz. Since the mean path of gravity is comparable to the regular separation of 18 mm between tiles, the response of the individual tiles is clearly visible. The calorimeter response is calculated using two methods. The first method referred to as the Integral Process is evaluated and divided by the corresponding size of the cell and the area of the curves for each cell. The cells on the boundary need a special procedure to understand the invisible tail and to correct the cross-talk between cells. This approach is approximately 0.2% accurate. Another method is the Amplitude Method in which the signal is placed on each tile with the tails in mind and the signal amplitude for each tile is given in the calorimeter. The accuracy is better than 2% for a single tile response and greater than 0.3% for the average amplitude of a cell. When comparing the two methods, the integral method is faster so that the cell response can be quickly equalized while the amplitude technique is used for detailed module quality scans [32, 33].

Chapter 4

The Online Software

4.1 The ATLAS Online Software

The ATLAS online software is a part of the Trigger and Data Acquisition (TDAQ) system. It is a software system that manages, controls and keeps track of the TDAQ system, excluding the transport and processing of the physics data. It is therefore the core system that combines the other subsystems, exists simultaneously and operates with the other subsystems in terms of the triggers, a uniform interface system, event-builder, processor farm, detector readout crate controller and DCS [25]. The online system consists of various components of which are listed below [25, 30]:

- Inter-Process Communication (IPC): The main component for contact. This depends on the transfer of the underlying TCP/IP message.
- Information Services (IS): The service which allows sharing between applications of any sort of user-defined data.
- Configuration Databases: File device design used to define the configuration.

- Process Manager: The system that is responsible for applying to the nodes.
- Access Manager: The network responsible for a given user's access to resources and nodes.
- Resource Manager: The resource allocation bookkeeping.
- Run Control: The core Finite State Machine (FSM) service in charge of the controlled application structure.
- Monitoring: The infrastructure for online monitoring.
- Integrated Graphical User Interface (IGUI): The user-friendly interface with the run control.
- Expert System: The service overseeing the actions of recovery.

The Graphical User Interface (GUI) used in the ATLAS online software system is the partition (see Figure 4.1). The partition is a software element with information regarding the software and hardware that can executed at a specific time. Each partition can only use one given resource only once, but multiple partitions can be run simultaneously as long as they don't use the same resources. The software description is done through the configuration database which relies on the Object Kernel System (OKS). The OKS is an object-oriented database with its storage based on XML [25].

Each of the four TileCal partitions (EBA,EBC,LBA,LBC) (See section 3.1) can be operated by TDAQ independently, as so called TTC partitions. This is because each partition is equipped with its own back-end electronics that make it possible for independent operation of the front-end. [15].

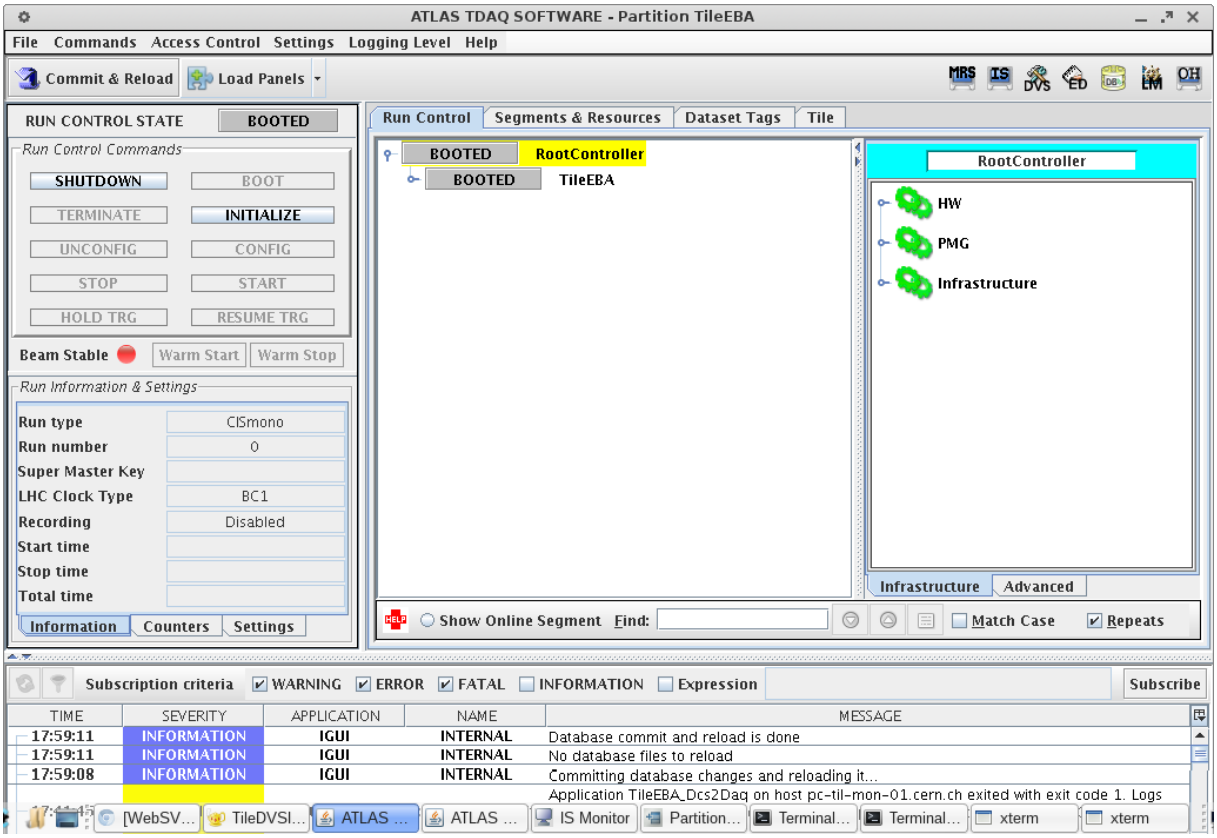


Figure 4.1: The ATLAS Partition [34]

Multiple TDAQ partitions can be employed at the same time depending on the maximum number of occurrences allowed for the resources in use. Some resources such as the detector instrumentation resources are created in such a way that allows them to have unique instances across all partitions. A super-drawer cannot be in the Finite State Machine (FSM) in two opposing states, but two super-drawers from two separate TTC partitions could be. There is one TDAQ partition in the database of the configuration which defines each TTC partition of the TileCal. The four TTC partitions, each identified in a different segment, are included in another TDAQ partition. This allows for easy swapping between the configurations [25].

4.2 The TileCal Online Software

The TileCal Online Software is a software used in the TileCal operation that is not provided by the ATLAS Online Software. It provides detector-specific software for the BE electronic crates, the calibration runs steering mechanism and infrastructure for handling calibration events during physics runs, hardware-level monitoring of software, so called Diagnostics or Detector Verification System (DVS) tests, and read-out system level monitoring. The software does not provide for Cs calibration scans that are done by specialized software derived from the TileCal online software. One of the key pieces of the TileCal online software is the ROD Crate DAQ.

The ROD Crate DAQ (see Figure 4.2) (RCD) framework is an extension of the ROS software that allows for the integration of handmade hardware into the general TDAQ software. The RCD is based on a multi-threaded readout application core that loads specific plug-ins at run-time to suit the specific needs of the detec-

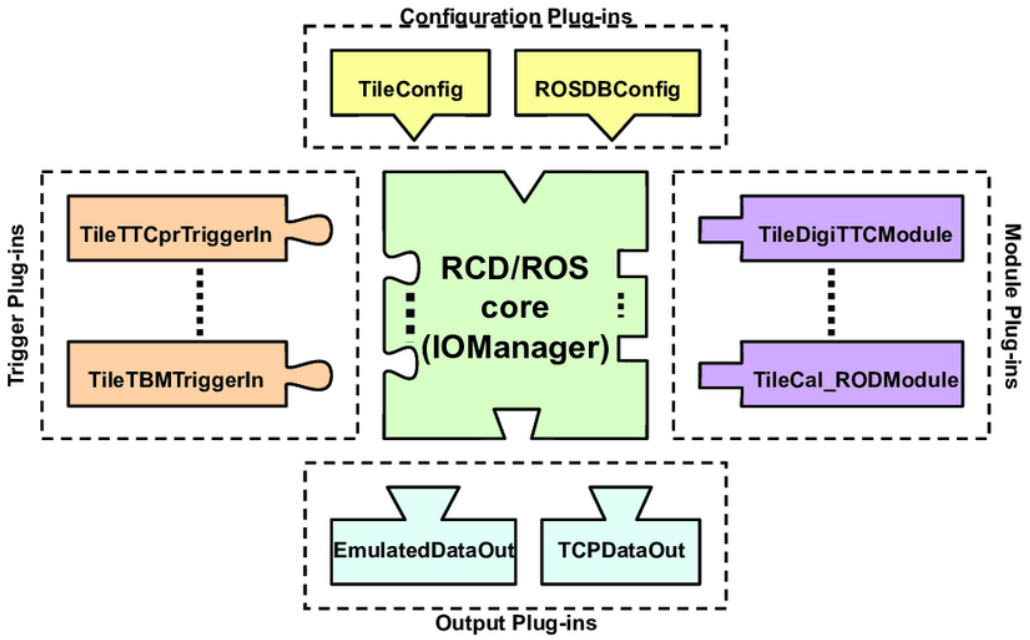


Figure 4.2: The ROD Crate DAQ [25].

tor. Various plug-ins are available for different purposes. A schematic overview of the application readout is displayed in Figure 4.2. The Configuration plug-in loads the configuration database information and transfers it to the core application of the RCD. The trigger plug-in manages data fragment requests. This operates on a request list as a separate thread that queues requests. A variety of RCD request handlers dequeue them by executing the requests for data that transfer the output information to the output plug-in. The module plug-in is a controlled resource that receives RCD commands for transformation. It does not send data to the output plug-in in the ATLAS activity mode. The output plug-in manages the data output that can be sent or written down to a file elsewhere through the ethernet [25, 30].

The run control service commands the RCD application. When the user sends

a command to run control transition through the IGUI, the RCD will receive a request for a state transition. The RCD responds to the request and operates the controlled hardware according to the specific code of the detector. The RCD required configuration is stored in the configuration file, which is an object-oriented database that enables object-to-object connections. To add an object to the database configuration, it must belong to a class specified in the schema. To describe the specific classes of TileCal, the basic schema is extended. The configuration database describes all hardware objects.

Most objects in the RCD inherit from the Readout Module. The RCD object represents an RCD application in the configuration database. It loads various plug-ins based on its attributes and relationships. The RCD recovers the class name of the associated objects and loads the plug-in library with the same name dynamically. A programming interface referred to as Data Access Libraries (DAL) is auto-generated from the schema classes in order to access the objects stored in the configuration database [25, 30].

4.3 The Diagnostics and Verification System

The Diagnostics and Verification System (DVS) is part of the ATLAS Online TDAQ software. It is a supporting structure that allows TDAQ developers and experts to combine tests and knowledge into it, thus making it user-friendly for a non-experienced shift operator to be able to diagnose problems within the TDAQ component. There are two types of TDAQ users namely the TDAQ operator and the TDAQ expert. The TDAQ Expert is mainly involved in the implementation, configuration and storing tests in the database while the role of the TDAQ operator is to perform tests on the components [35].

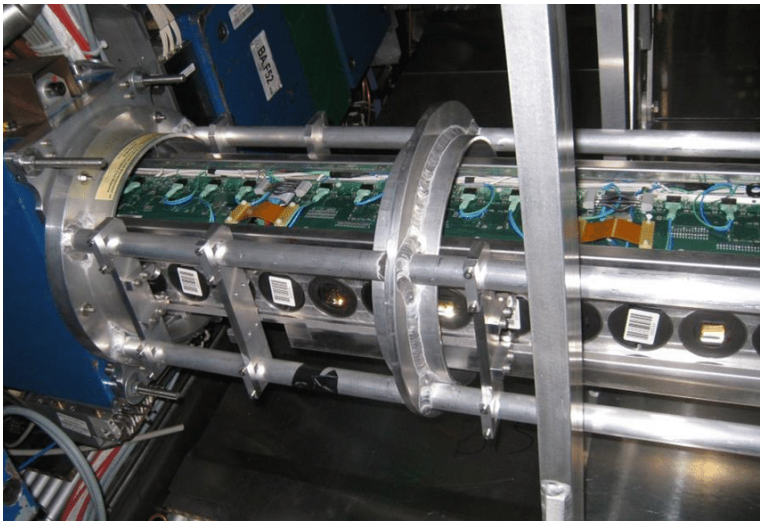


Figure 4.3: The TileCal super-drawer extracted from the module [36].

The DVS tests are a set of digital checks that examines the functionality of the components of the super-drawer (see Figure 4.3). They are similar to the Mobile Drawer Integrity Checking System (MobiDick) in the sense that they check the functionality of the individual components of the super-drawer. the MobiDICK and DVS tests differs in aspects of how the test is being performed. For the MobiDICK testing the drawer has to be opened while the drawer has to remain closed for the dvs testing. DVS are second level tests that follows immediately after MobiDick to verify the faults found in the components [35].

The DVS can be accessed by users (TDAQ operator) via the DVS Graphical User Interface (GUI) or by online software packages (TDAQ supervisor) via the Application Programming Interface (API). To be able to implement the required functionality, the DVS reads the TDAQ configuration via the configuration databases service, it then launches the tests via the test manager and then use the CLIPS ("C" language Integrated Production System) packages to implement the expert

system [35]. The DVS has an internal architecture that is composed of the following:

- A Test Repository Database: A database that describes the attributes of a test in the configuration database. The test attributes are described in the form of classes in this case the classes are *Test, Test4Object or Test4Class*.
- A knowledgeable Base: Store specific Knowledge about component functionality.
- An Expert System Engine: Available via the C/C++ API.
- C++ and Java Libraries.
- A GUI application: The user interface used for DVS is the partition. The hardware components are described in the configuration database of the ATLAS TDAQ. Tests are configured using the Test Manager which reads the configuration database to select tests to be executed. Tests have to be collected in Test Repositories and linked to the Partition or one of its Segments [35]. The user can select any component on the partition and perform tests specific for that component.

DVS package internal architecture (see Figure 4.4) for end users (TDAQ Operator or other Online SW component like the Supervisor application), DVS provides the possibility to have a testable view on a TDAQ configuration, where a user can select a single component or a group of components and verify its status. This functionality is provided via GUI, or via the C++ and Java.

4.3.1 DVS Tests

There are several types of DVS tests:

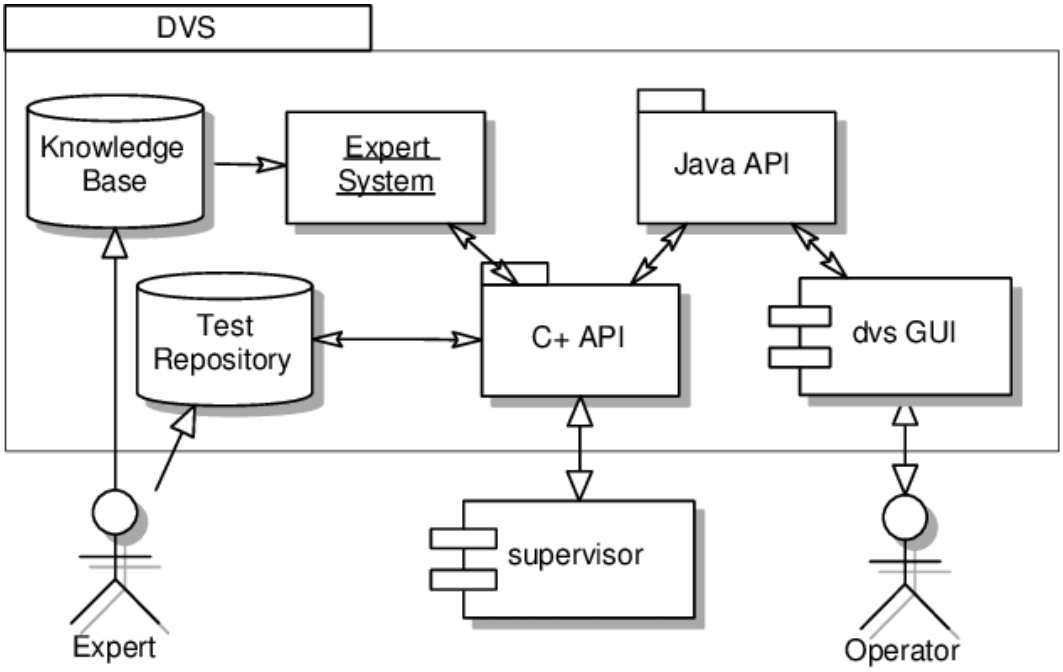


Figure 4.4: DVS internal architecture package for end-users [35].

- CIS: This test checks the existence of a pulse inside some bands for high and low gains.
- Pedestal Test: This test checks the low and high frequency values and compares it to nominal values.
- DMU Memory: This is a test whereby a bit-wise pattern is written to the DMU memory and then pattern data is read out and checked for errors.
- Stress: This is a test whereby a 100 kHz random trigger and a full busy logic is used to reject the acquisition. Data is processed inside the Digital Signal Processor. The number of the Cyclic Redundancy Check (CRC) errors found in the data is reported.
- Digitiser Address: The test checks the correct address of the digitiser board [34].

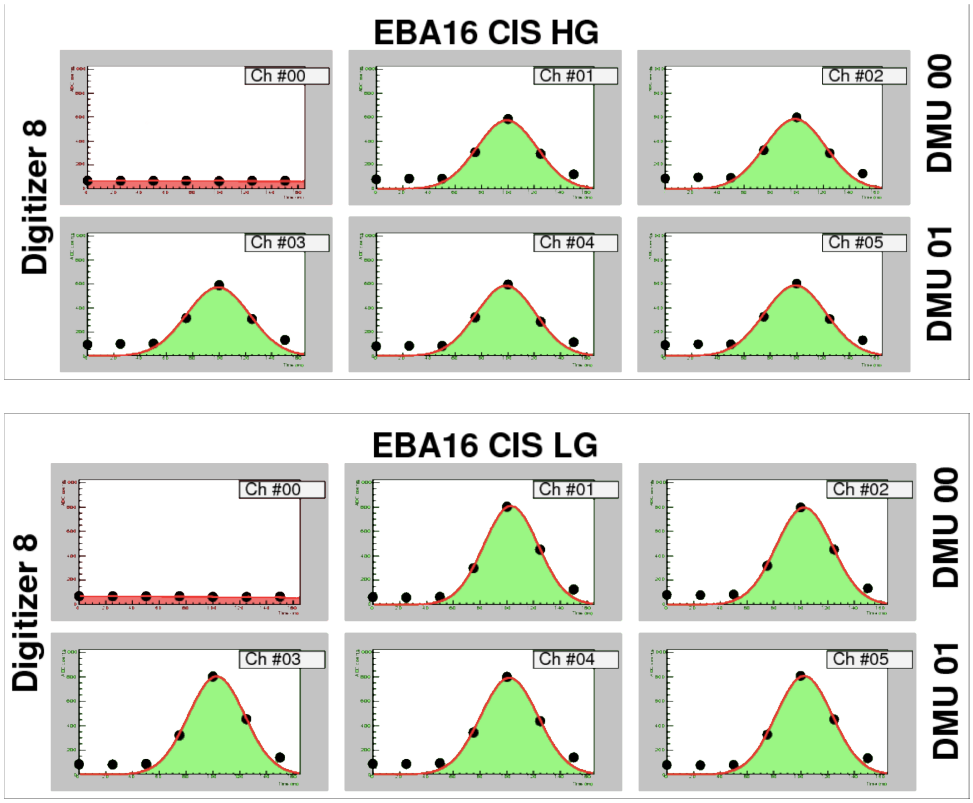


Figure 4.5: Charge Injection Scan plots for EBA16 in both Low and High Gains.

Although there are a number of the DVS tests, the TDAQ experts focus only on the CIS and Pedestal tests. In this section the plots were made by the author by making use of the existing DVS codes for the CIS and Pedestal tests. Figure 4.5 displays the results for the CIS DVS test for the sixteenth Extended Barrel (EBA16) module in the low and high gain.

For the purpose of simplicity a gaussian function is fitted through the samples for pulse recognition. The plots are also color coded, green means everything is fine, and red means that something is wrong with that particular channel i.e channel 0. A channel is associated with the PMT number and the DMU. Finding a problem in a certain channel makes it easy to determine which electronic is

faulty. After testing the module using DVS, the module is repaired and tested again to confirm the repair [37].

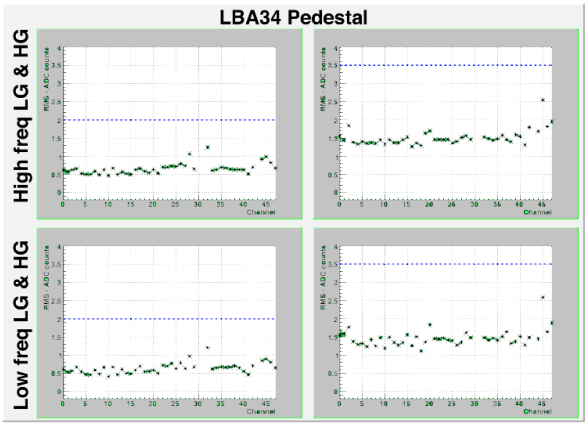
The low and high gains refers to the Analogue to Digital Converter (ADC) gains. The gains are chosen automatically by the DMUs. If the number of ADC counts in High Gain (HG) is 1023 for at least 1 of the data samples, then the gain is switched to Low Gain (LG). If the number of ADC counts in HG is 0, then the gain is switched to LG [37].

Figure 4.6 displays the high and low frequency noise for the Long Barrel number 17 and 34 (LBA19 and LBA34). LBA19 had a bad response in both the low and high gains. LBA34 had a good response in both gains.

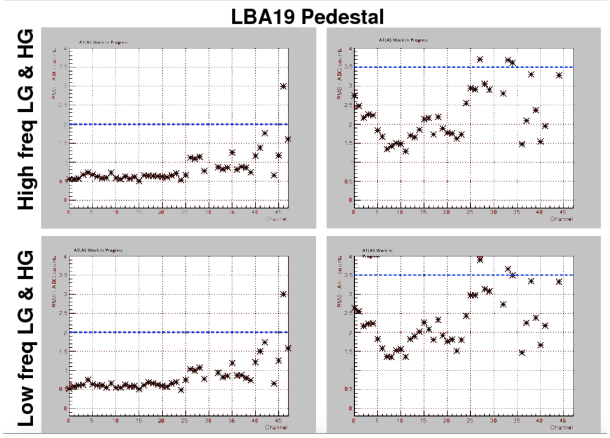
4.3.2 Future Plans with DVS

The DVS testing system has fewer tests compared to the MobiDICK, so more tests need to be implemented to make the DVS complementary to the MobiDICK tests, once the super-drawer has been closed into operation mode. The tests that are yet to exist in the DVS tests are the stuckbit tests that already exists in the MobiDICK system. Considerable progress was made in this area, and although prospects are good for the near future, clear effort is needed. The Diagnostics and Verification System (DVS) is part of the ATLAS Online TDAQ software. It is a supporting structure that allows TDAQ developers and experts to combine tests and knowledge into it, thus making it user-friendly for a non-experienced shift operator to be able to diagnose problems within the TDAQ component. There are two types of TDAQ users namely the TDAQ operator and the TDAQ exper

The Diagnostics and Verification System (DVS) is part of the ATLAS Online TDAQ software. It is a supporting structure that allows TDAQ developers and



(a)



(b)

Figure 4.6: Results for the high and low frequency noise pedestal tests in every channel.

experts to combine tests and knowledge into it, thus making it user-friendly for a non-experienced shift operator to be able to diagnose problems within the TDAQ component. There are two types of TDAQ users namely the TDAQ operator and the TDAQ exper

Chapter 5

Requirements for the HL-LHC

The LHC plans to increase the current luminosity to become the High Luminosity LHC (HL-LHC) (See Figure 5.1) which will create more opportunities in the search for physics beyond the SM. The LHC is mainly designed for the discovery of new physics through proton-proton collisions at a center of mass of 14 TeV and a luminosity of 1×10^{34} cm^{-2} s^{-1}. The LHC plans to increase the luminosity to up to 7.5 $\times 10^{34}$ cm^{-2} s^{-1}, which corresponds to an increase in the number of simultaneous proton-proton interaction per bunch crossing of up to an average of 200. The LHC has managed to achieve the instantaneous luminosity of 2.06 $\times$ 10^{34} cm^{-2} s^{-1} in 2017 [38]. The LHC is currently undergoing Long Shutdown 2 (LS2), which will last until early 2021, during which the injectors will be upgraded to prepare for the luminosity increase and Run 3. During the LS3, which will take place between 2025 and 2027, the interaction points will be upgraded by the installation of new elements, including new focal magnets and crab cavities. All of the equipment needed for the HL-LHC, and its experiments will be installed during LS3 [39]. The increased luminosity of nearly a magnitude above the original design will lead to an increase in the particle flux in the detector, requiring an upgrade of almost all ATLAS detector systems. The increase in the



Figure 5.1: HL-LHC Timeline [41].

number of collisions per bunch crossing will cause a deterioration in the performance of the ATLAS detector. However, an upgrade in the calorimeters, trigger system, inner tracker and muon spectrometer readout electronics will improve the performance. The TileCal was designed 25 years ago but has only been in operation for the last 10 years, using the technology or electronics provided at the time. The electronics are outdated, and they are becoming more difficult to use and costly to maintain. This means that modern electronics that can provide faster and high-precision measurements are required [3, 40].

5.1 The Trigger and Data Acquisition System

The TDAQ system (see section 2.4) of the ATLAS detector is being redesigned completely pending the upgrades. The redesign of the trigger system is currently being considered in two scenarios namely a single-level (L0) and a two-level trigger (L0 or L1) system. The starting point for the HL-LHC is the L0 trigger system

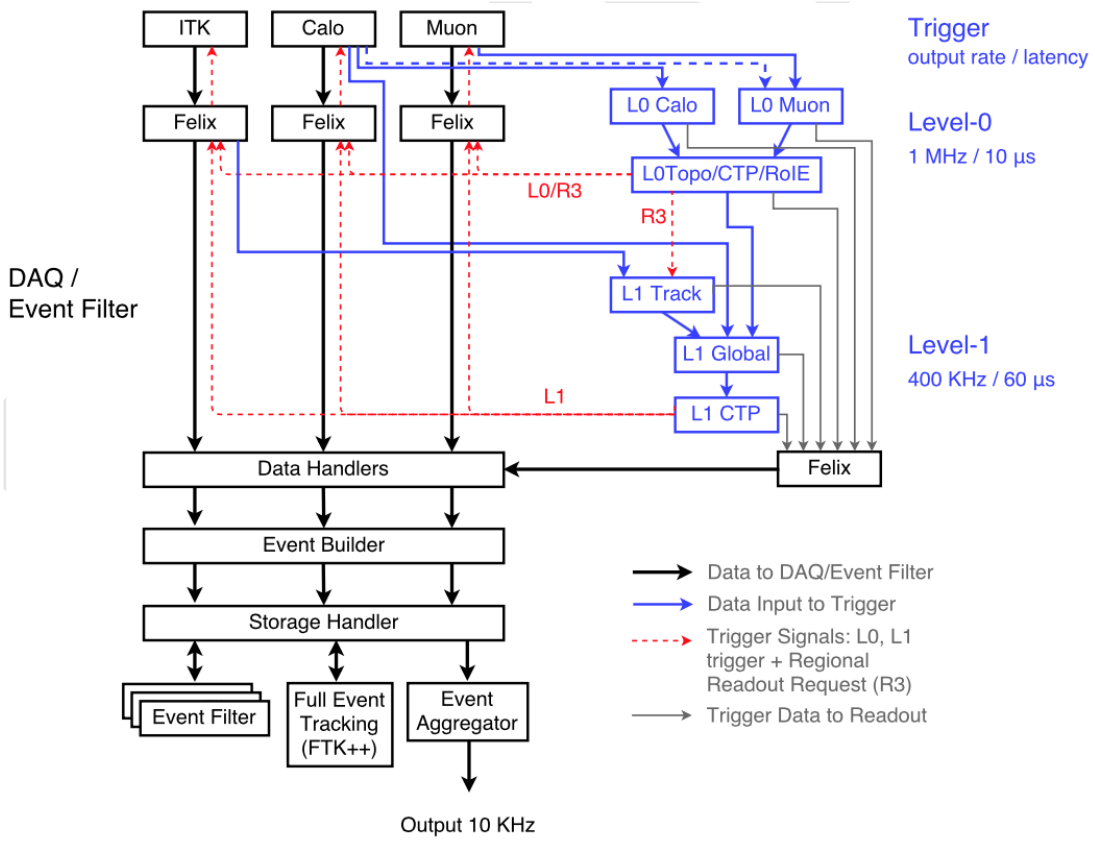


Figure 5.2: High level overview of the trigger and readout structure of the HL-LHC framework with two Level-0/Level-1 ATLAS triggers [3].

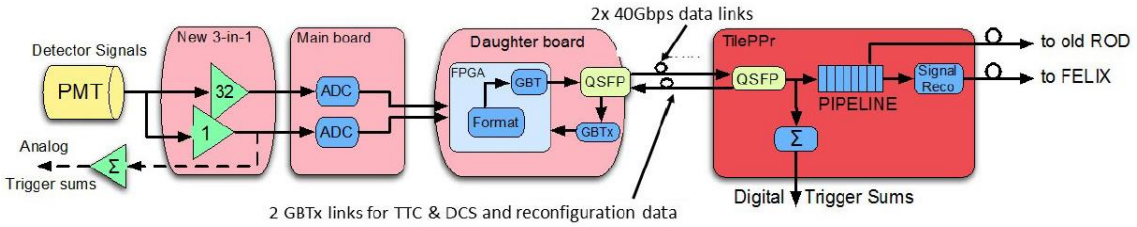


Figure 5.3: Schematic signal and data path for the upgraded TileCal. Shaping is carried out in the front board on a PMT frame, Main-board digitisation, high-speed Daughter-board communications. The off-detector Pre-Processor (PPR) processes and transmits data to the DAQ system and triggers TDAQi module processors [3].

and a possible evolution to the L1 system is predicted in a second phase. Figure 5.2 displays the High-Level description of the new trigger system design [42]. For the TileCal, the two systems are not drastically distinct, this makes the evolutionary transition between them much easier. The TDAQ architecture of the entire ATLAS detector anticipates a fully digital calorimeter trigger that has a higher granularity and higher precision compared to the current TDAQ system. The L1Calo in the current TDAQ scheme uses analogue signals that corresponds to the pseudo-projective towers of 0.1×0.1 in $\Delta\eta \times \Delta\phi$. The pseudo-projective towers in the The PMT signals are adjusted approximately in time using delay lines but not calibrated to account for gain differences in electronics. In the TileCal, the tower signals are built from the summation of the PMT signals by making use of the analog summing boards. The PMT signals are adjusted approximately in time using delay lines but not calibrated to account for gain differences in electronics. The summing board output are then sent off-detector to the trigger Pre-Processor (PPR) system by using 30 m to 60 m long cables. The analogue system in the upcoming upgrades will be replaced in such a way that all the information from the TileCal cells will be sent to the trigger system at a rate of 40 MHz with a maximum latency of about 1.7 μs [3, 42].

Downlinks	**Present**	**Upgrade**
Number of fibres	256	1024
Link Bandwidth	80 Mbps	4.8 Gbps
Uplinks	**Present**	**Upgrade**
Number of fibres	256	2048
Link Bandwidth	800 Mbps	9.6 Gbps
Back-end readout modules	32	32
Back-end crates	4 (VME)	4 (ATCA)
Back-end Input bandwidth	6.4 Gbps	625 Gbps
Back-end output bandwidth to DAQ	3.2 Gbps	40 Gbps
Back-end output bandwidth to trigger	Analogue FE	$\sim$ 500 Gbps

Table 5.1: Comparison of the present (ROD) and the PPR upgrade architectures of the TileCal BE readout. The redundancy and backup data links are not included. The system has a total number of fibers twice that indicated here.

The transmission of all information requires a significant increase in the bandwidth of system data, as seen in table 5.1. Each of the 256 optical links that runs at 800 Mbps will now have to run at 38.4 Gbps to transmit all the samples out from the front-end. This is realized by splitting each link into 4, and thus running 1024 links from the front-end each one running at 9.6 Gbps.

The new trigger system design will have access to the digital data from each calorimeter cell with low electronic noise levels and precise energy measurement. Numerical precision, calibration accuracy and equivalent noise characteristics of the current information should increase the selectivity of the trigger. The data pipelines are on the detector in the current system; thus, the trigger accept signals must be propagated to the electronics at the FE. The transmission delay is approximately half of the current 2.5 μs latency of the first level trigger. In the upgrades, the maximum latency trigger ATLAS L0 will be increased to cope with the higher pile-up while retaining the L0 trigger at a reasonable rate and good performance. For the upgraded architecture, including the pipeline buffers, the BE PPR system is shown in Figure 5.3; it will be placed closer to the trigger system to reduce latency due to delay in signal propagation. The propagation of

the off-detector detector signals is similar to the current method, but with the new architecture, the transmission of the L0/L1 approval signals to the pipelines is significantly reduced [42]. At the LHC the bunch crossing rate, the pulses from the PMTs are conditioned and digitised in the FE boards and continuously transferred off-detector to the PPR module using an optical link interface board called the Daughter-board. The PPR stores the ADC information in pipeline memories and processes the data simultaneously by planning optimised primitive triggers. The trigger primitives are the energy measured in towers and cells of pseudo-projection, they are transmitted at each bunch crossing to the L0 trigger processors with a delay of 1.5 μs. The reconstructed energy, time and quality factor for each cell will be sent to the data network (FELIX) for event aggregation and storage upon receiving the L0 and or L1 acceptance signal [3].

5.2 Radiation Hardness

As explained in Section 2, the TileCal readout electronics are stored in the outer radius of the calorimeter and shielded by the body of the calorimeter, so that the radiation dose requirements are not as critical as in other ATLAS sub-detectors. However, the expected increase in HL-LHC particle fluxes requires that the current electronics be replaced because many on-detector components will not withstand the projected HL-LHC radiation dose. A maximum Total Integrated Dose (TID) of 244 Gy is estimated at the HL-LHC over 10 years of operation in the most critical areas as seen in Figure 5.4. This figure takes into account the safety factors used to describe the uncertainties in the simulation of particle fluence and the low rate of accumulated dose; this is an order of magnitude greater than that used in current electronics.

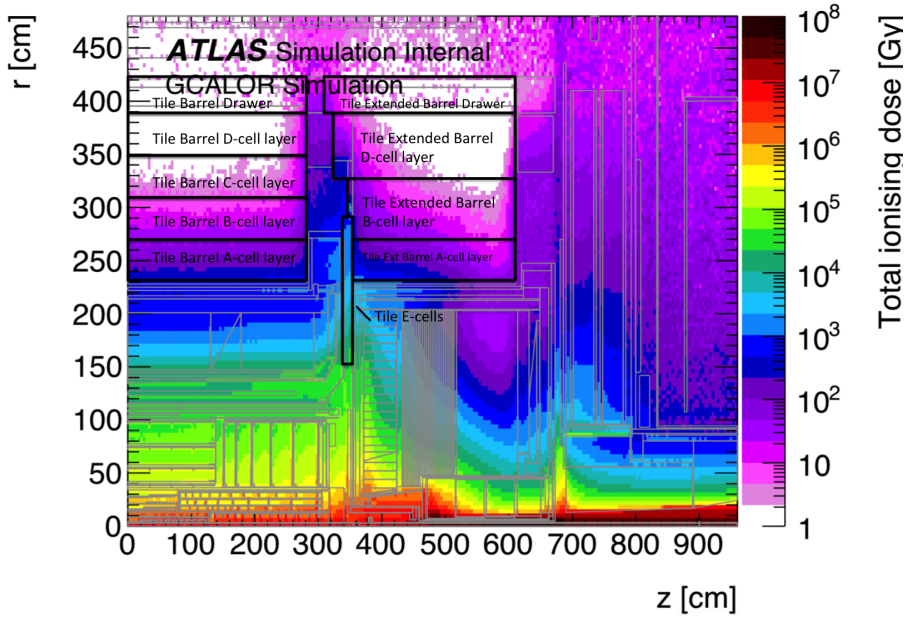


Figure 5.4: Total dose of ionization in Gy/4000 fb^{-1} in the upgrades of the ATLAS tracking and calorimeter areas. The minimum bias pp events in 14 TeV center of mass energy, assuming a total inelastic section of 80 *mb*, are simulated using Pythia8. The GEANT3/GCALOR code simulates partition tracking and material interactions [3].

	Zlo	Zhi	Rlo	Rhi	TID	NIEL	SEE
On-detector electronics	**cm**	**cm**	**cm**	**cm**	**GY**	**n/cm^2**	**h/cm^2**
High voltage	275	275	410	410	10	1.32×10^{12}	2.31×10^{11}
Main-board	275	275	400	400	10	1.03×10^{12}	2.46×10^{11}
FE board	270	280	400	410	10	1.03×10^{12}	2.46×10^{11}
Daughter-board	210	240	400	400	2	2.44×10^{11}	1.50×10^{10}
LVPS - Barrel	275	300	390	400	24	1.77×10^{12}	4.20×10^{11}
LVPS - End-cap	610	635	390	400	4	2.40×10^{11}	5.64×10^{10}
Scintillators							
E3	353	354	184	228	6.88×10^3	1.36×10^{14}	1.92×10^{13}
E4	353	354	147	184	2.1×10^4	2.81×10^{14}	5.08×10^{13}
E4'	353	354	131	147	2.36×10^4	3.31×10^{14}	6.00×10^{13}
MBTS	355	357	13	89	1.46×10^6		

Table 5.2: Simulated radiation doses for 4 ab^{-1} of HL-LHC running.

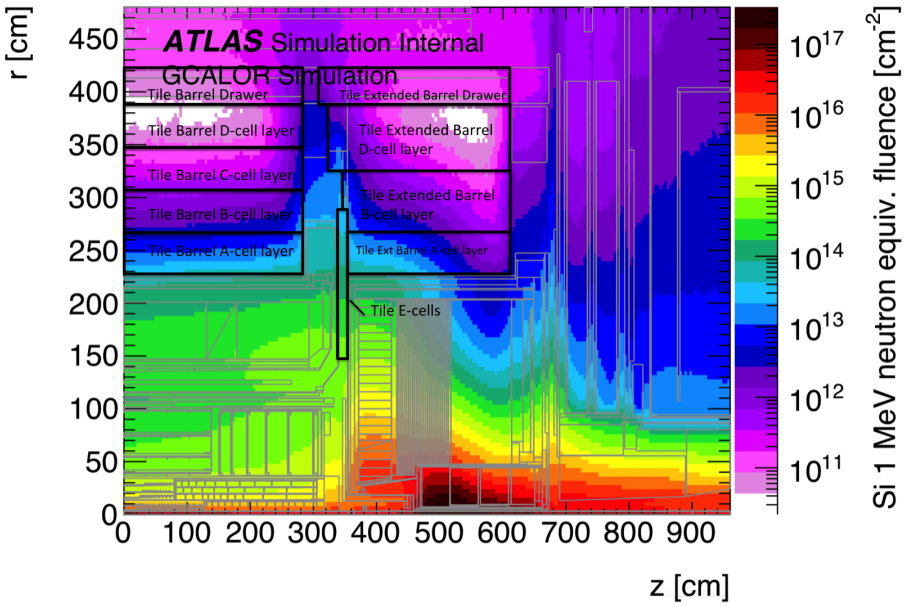


Figure 5.5: Silicon displacement damages, expressed as a fluence of the equivalent of 1 MeV neutrons for an integrated 4000 fb^{-1} luminosity, respectively. Pythia8 simulates the minimal pp events at 14 TeV centers of mass energy assuming a cross section of inelastic 80 mb. The GEANT3/GCALOR code simulates particle tracking and material interactions using the latest ATLAS detector geometry description. In azimuth and around $z = 0$ the geometry model is symmetric [3].

A Non-Ionizing Energy Loss (NIEL) equivalent of 6×10^{12} (1 MeV) neutrons/cm^2 over 10 years is projected for the displacement damage as seen in Figure 5.5. From Figure 5.6 the Single Event Effects (SEE) are evaluated taking into account an expected fluence of 1.5×10^{12} hadrons/cm^2 over a period of 10 years.

Table 5.2 gives a more detailed information about the location of the on-detector electronics and the simulated dose for the whole HL-LHC program for the electronics and scintillators that are most exposed. Table 5.3 gives the associated safety factor multipliers, as specified by the ATLAS Electronics Coordination Group. In the current readout system, the data from each bunch crossing will be processed on-detector using electronic pipeline until the trigger to be sent off-

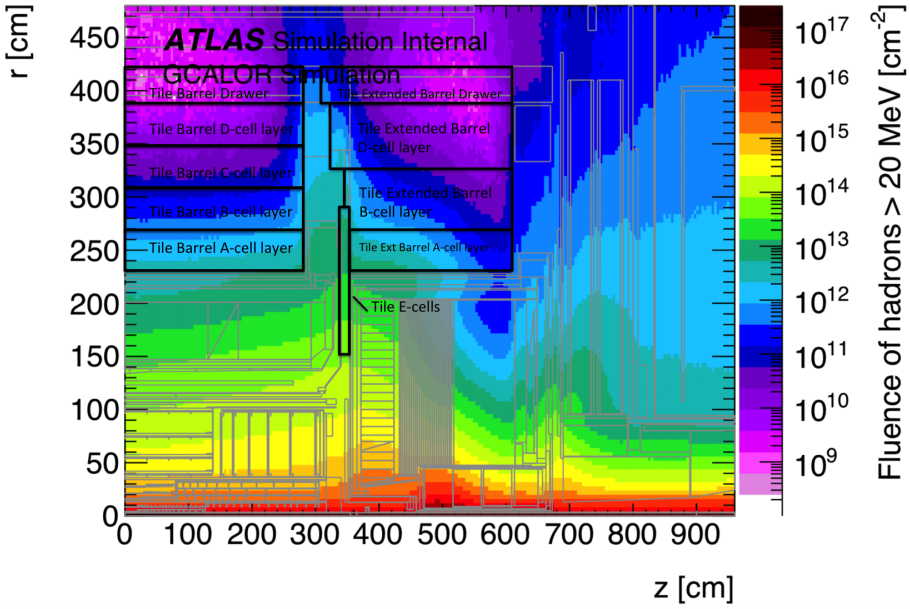


Figure 5.6: Total fluence of hadrons with E $>$ 20 MeV per cm^2 for an integrated luminosity of 4000 fb^{-1}. The minimum-bias pp events are simulated with Pythia8 at the 14 TeV center of mass energy assuming an inelastic cross-section of 80 mb. Particle tracking and material interactions are simulated with the GEANT3/GCALOR code using the latest geometry description of the ATLAS detector upgrades [3].

Safety Factor	Simulation	Enhanced Low Dose Rate		Lot Variation	
		(no anneal test)	(no anneal test)	(ASIC)	(COTS)
TID	1.5	5	1	1	4
NIEL	2	1	1	1	4
SEE	2	1	1	1	4

Table 5.3: Safety factors multipliers for radiation certification of ATLAS electronics.

detector selects one specific bunch crossing. The new design is important due to the large rise in SEE in the electronic pipelines and has an additional advantage of constantly digitising and transmitting off-detector data using high-speed optical links. The vulnerability of FPGAs and other components in the Daughter-board to single-event upsets will be reduced using a triple redundant framework for memory and logic configuration [3].

5.3 Accessibility to the Electronics

Another common problem faced in the upgrade and operation of the ATLAS detector at the HL-LHC is the activation of the detector. Therefore, the upgrade and maintenance work will have to be analysed and optimised according to the As Low As Reasonably Achievable (ALARA) principle. The rules of CERN on radiation protection clearly states that the maximum dose exposure allowed for a professional worker should be less than or equal to 6 mSv/year and 2 mSv/month. For the simplicity of installing, maintaining and manipulating the super-drawer, the new super-drawer design is split into four mini-drawers. The splitting of the super-drawer will improve access to the electronics. This will allow for easy installation and maintenance operation in all scenarios of the detector opening, thus avoiding the current situation in the standard small opening where the super-drawers in the current EB modules cannot be fully extracted.

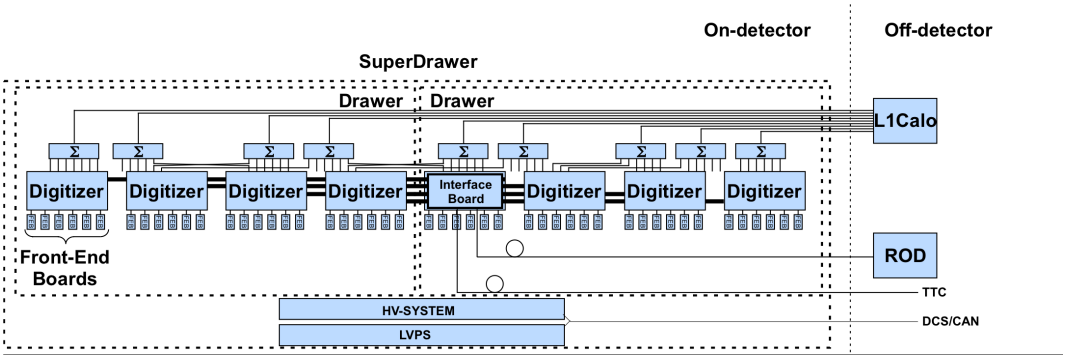


Figure 5.7: The configuration of the present readout electronics (Run 1) [3].

5.4 The Reliability and Redundancy

The detector operations during Run 1 and Run 2 gives valuable information on what is needed to improve the reliability of the electronics and how to limit the influence of component failures on the data quality. In the current detector, the super-drawer is the basic readout unit, it is supplied with an independent data link, a TTC link, power lines, cooling and monitoring services [3]. During Run 1 the most important failures were due to the power distribution; the finger low voltage supply failures, the DC/DC converter stage installed on the detector, the failures in the power distribution in the interconnected optical interface cards, the digitisers and the mother-boards. The power distributions in the super-drawers displayed a significant voltage drop that had a severe impact on the range of proper operation of critical components like the TTCrx. Other failures were also observed in the HV distribution to the PMTs. The above failures were reduced by a consolidation campaign (see Figure 5.7) that was held during the LS1 in 2013-2014. Other failures worth mentioning was a failure in the cooling circuit and the links in the optical interface card. The failures described above result in having a dead region in the detector of about 24 cells covering an area of 0.7 $\times$ 0.1 radians in $\Delta\eta \times \Delta\phi$. To reduce the impact of such failures, the upgrade system will be partitioned into smaller independent readout units [3].

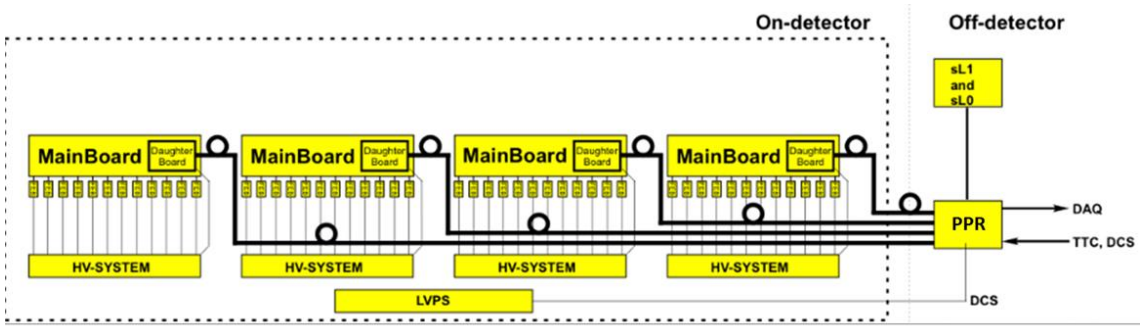


Figure 5.8: Organization of the readout electronics in four HL-LHC separate mini-drawers [43].

Figure 5.8 demonstrates the overall structure of the new super-drawer with four different readout parts, the mini-drawers. Every mini-drawer accommodates up to 12 PMTs, FE boards and all related service boards. Logically, the mini-drawer is divided into two independent sides, each with independent power, data links, and monitoring services. In this scheme, each cell is read out by two separate PMTs with power, services and data connections that are completely redundant to BE electronics. There should be no failures in the redundant power distribution scheme. However, in the worst case, one-eighth of the area affected by a malfunction in the current system would be the dead zone. There were other major failures in the interconnection between boards. The latest electronics are arranged in various boards and mezzanines, therefore, the mechanical and electrical interconnections consistency over the 3 m long unit is a weakness. Because of the partitioning of the functions of mezzanine cards, the stacking of boards and all interconnections must be avoided as much as possible in order to boost the long-term performance.

Certain failures found during Run 1 were single-channel failures, often due to the failure of ADCs or the failure of opto-couplers in the HV regulation board or the

capacitor in the PMT HV dividers. Apart from the capacitor in the HV dividers, the reported single-channel failures do not have major impact on the physics performance. Sometimes this result in a short circuit that could jeopardize the operation of the neighboring PMTs since the granularity is grouped together in the HV input order. The other thing about the new electronics is that they've been in use for a long time, so they're getting older. [3].

5.5 The Optics Robustness and PMT stability

After a detailed study on the aging and radiation sensitivity of scintillating tiles, WLS fibers of all PMTs, it was determined that there was no need to replace them. This study was carried out by observing the evolution over time of the performance of these active elements during normal operation and verified by the irradiation tests of the scintillator in the laboratory during production. Using thorough extrapolation, the studies predict that the scintillator equips the most exposed cells within the EB thereby resulting in light loss that is slightly lower than 5% (10%) after 300 fb^{-1}. Such variations would be easily rectified with the calibration systems. There is no strong concern based on these trials regarding the light loss of the scintillator which increases radiation in regular TileCal cells. However, the gain drift of the PMT had to be carefully measured. This was done by measuring the response after long time exposure of the PMT installed in the detector (R7877) and the newest model from Hamamatsu (R11187). In these studies, both PMTs resulted in t a drift of 0.1% in the gain for each Coulomb of integrated charge at the anode. Which is similar to the one observed on the detector during Run 1 and 2.

An important observation is the fact that each tested PMT group shows a large

spread in the individual drift with time. After a 500 C integrated anode charge, the spread the exceed ± 25% of the average value. Conservative projections of the expected global loss of HL-LHC irradiation show that a significant degradation will likely occur only in most exposed, low-radius and high-speed cells (8% of total PMTs). Laboratory tests were performed on 20 latest generation PMTs (model R11187) and a sample of 10 PMTs (model R7877) disassembled from the detector during the 2017 maintenance period. Measurements have shown that the latest PMT design has significantly improved amplification stability as a function of time, resulting in a very promising alternative to the current PMT model (R7877). The replacement of these 768 PMTs protecting the most exposed cells is included in the TileCal phase-II upgrade [3].

5.6 Mechanics

The super-drawers currently in use will be replaced with structures a quarter as long. This move is deemed necessary to enhance the performance of the existing drawer cooling system and to allow for easier access to electronics advised by ALARA (see section 5.3) when opening the detector, for which the end-caps of the detector will only have to move by half the distance [3, 42].

5.6.1 The Mini-drawers and Installation

The new mechanical structures proposed for the upgrades are called the mini-drawers. For the upgrade system, four mini-drawers will make up a super-drawer, where each mini-drawer consists of its own power and independent signal path to the BE electronics. A single super-drawer will consist of three types of mini-drawers, which are similar in terms of mechanical structures but slightly different due to their position in the super-drawer. The most important elements in the

mechanical structure of the mini-drawer are: the mini-drawer body, the sliding plates, the mechanical links, the hydraulic connectors, brackets and the cooling bridge [42]. The mechanical structure for mini-drawers provides electric and optical services consisting of specific routes and cables and optic fiber connections. Mini-drawer prototypes have been designed and tested in a comprehensive manner to verify the expected results. The testing program evaluated the functions and operation of the mini-drawers, including the installation of all FE electronics and PMTs. The full super-drawer was installed into the actual TileCal wedge in Building 175 (at CERN) under practical assembly conditions.

A new installation tool has been developed for easy extraction and insertion of the super-drawers into the TileCal. The new tool is being tested during the demonstrator prototype tests. The new tool concept consists of three key elements, such as baskets, sliders and spools. Baskets are necessary for securing and assisting the insertion and removal of a mini-drawer during handling, while sliders are required to extend the girder rings inside the finger with respect to guiding axes and spools are required during mini-drawer installation in the TileCal module to provide distribution of electrical and optical services.

5.6.2 The On-detector Electronics

The mini-drawer contains up to 12 PMT blocks, where each PMT block consists of a light mixer, 3-in-1 card, an active HV divider and a PMT. The constituents of the PMT block are then connected to the Main-board (see Figure 5.9) that supplies them with low voltage and controls the 3-in-1 cards, it digitises their signals, transports the data to the Daughter-board link.

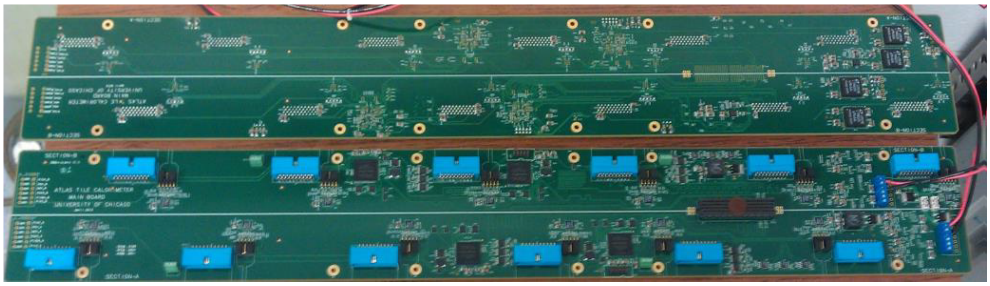


Figure 5.9: The Main-board [2].



Figure 5.10: The Daughter-board for the upgrade system [2].

The Daughter-board (see Figure 5.10) oversees the high-speed communication with the BE electronics. The mini-drawers also contains the HV distribution cards that receives the individual HV levels from each PMT via separate cables from a multi-channel off-detector HV supply. The on-detector TileCal structure is shown in Figure 5.11 [3, 44].

The overall design of the mini-drawers strongly emphasizes on reliability through redundancy and simplicity. In addition to the implied redundancy enabled by reading two PMT channels on each cell, low voltage distribution redundancy is made easy by splitting each mini drawer into small, separating units. Figure 5.12 shows the PMT block with its new constituents.

With the 3-in-1 FE card, high and low gain PMT signals (with a gain of 32) are amplified, gains are achieved, and CIS calibration is provided. One additional

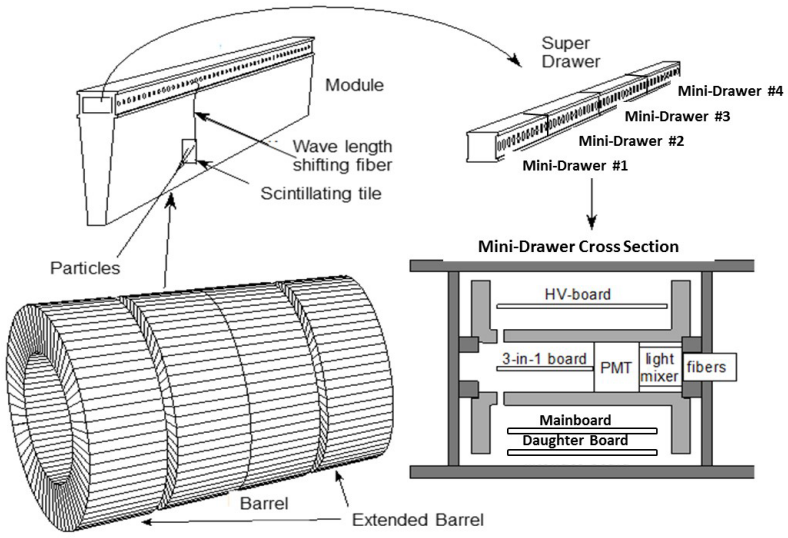


Figure 5.11: The TileCal and the on-detector drawers [3]. As mentioned in section 5.1, the links to the FE will arrive to the DB which is equipped with GBTx to decode the commands, and extract the system clock. Additional redundancy is achieved by duplication of the links, such that the back-end electronics can switch between the links in case of error.

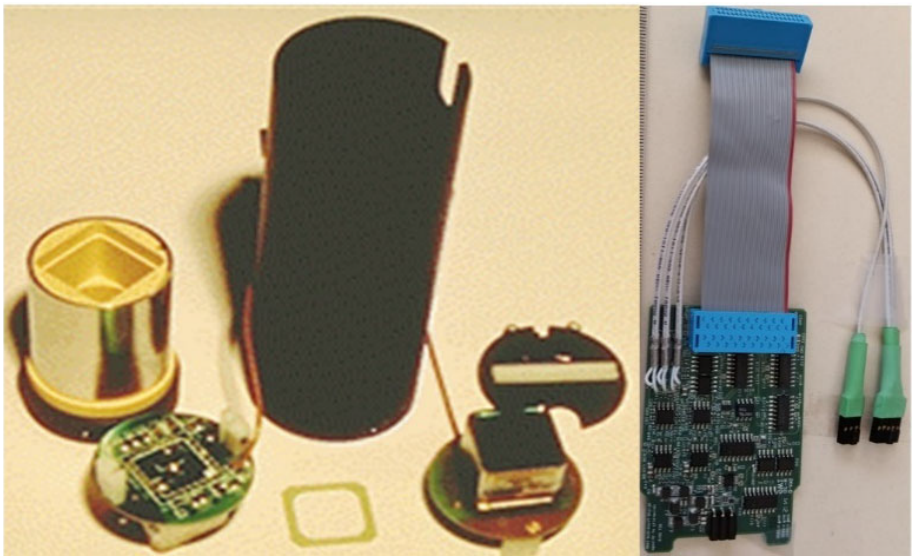


Figure 5.12: The assembly of a PMT block with the new constituents [3].

function is to integrate and digitise the current from a minimum bias event or a calibration capsule from a Cs source that can be moved via hydraulic pipeline cells. Each raw data from each PMT is digitised with an active dynamic range of 17 bit and sent for processing and data acquisition at the off-detector electronics. The 3-in-1 cards have discreet components and are a revised model with an improved linearity and noise level efficiency [42].

5.6.3 The Low and High Voltage Power Supplies

The TileCal Low Voltage Power Supply (LVPS) system provides power to all FE electronics, it also provides feedback and control via a monitoring system. Each super-drawer is powered by one LVPS box, which means that one LVPS box will power up four mini-drawers for the upgrade system, resulting in a total of 256 LVPS boxes for the entire TileCal. The components of the LVPS box are: eight individual power supply regulators called bricks, a fuse board, a monitoring/control board and a cold plate running sideways through the center of the water-cooled LVPS container. The LVPS box is powered by the 200 V circuit supply that resides at the USA15 cavern. The LVPS in the current system consists of eight types of bricks that are different in terms of voltage and current [3].

The new brick design for the upgrade system is similar to the current design in terms of the box structure, water-cooled cold plate and simple footprint of the brick used in the upgraded system. The new design will be different from the current design in terms of: the new design will have single type of brick that will convert the 200 V into 10 V output, the other significant difference is that the redundancy will be included in the design so that the eight bricks will be included in four sets of two. The current monitoring and control system of the LVPS

makes use of the Embedded Local Monitoring Board (ELMB) that is mounted on top of a custom mother-board with 32 analog inputs, 8 analog outputs and 8 digital outputs. The new LVPS monitoring system is being designed for the next generation but will use the new ELMB version of CERN. A prototype of 10 V bricks LVPS box was completed successfully and it was used in the three previous TileCal TBs in 2016 and 2017 [3, 42].

The HV system must provide individual power to almost 10000 PMTs, monitor the voltage for each PMT, and report the values to the DCS system. The HV system follows the design of the existing system, with a single primary HV feeder and an HV control panel that regulates individual high voltages for 32 or 48 PMT. In the current system, the HV control panel (called the HVopto) inside the detector minimizes the number of cables used to supply the primary HV detector (one per partition, i.e. a total of 256 driver pairs). The new system includes the HV regulation board, now referred to as HVremote, located outside the USA15 cavern, which allows easy access for maintenance at the price of a much larger number of cables. The current monitoring system based on HV-micro and CANbus, will be replaced by standard Ethernet. The HV prototypes have been implemented and the performance was tested in the laboratory and in TBs with an adaptation of the existing HV system [3, 42].

5.6.4 Off-detector Electronics

The structure of the DAQ of the TileCal HL-LHC is such that the digital samples of the PMTs are transferred to the TileCal Pre-Processor (PPR) bunch crossing. The data signals are stored in the PPR pipeline buffers and awaits a trigger decision, while in parallel, the PPR provides reconstructed data to the trigger system at 40 MHz. The reconstructed data consists of calibrated energy per cell or cell

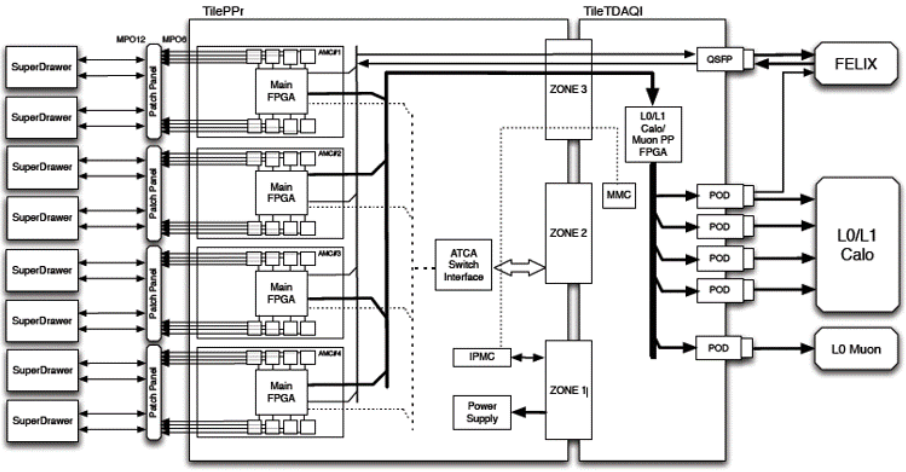


Figure 5.13: A functional block diagram for the Back-End electronics [44].

group, depending on the device trigger. For certain areas of the detector, the PPR system offers many copies of the data. The selected data events are then transferred to the FE Link Exchange (FELIX) device following the L0 trigger accept [3].

ATLAS selected the Advanced Telecommunications Computing Architecture (ATCA) to replace the VME bus as the base for modular electronics of the upgrade system. The ATCA blade form component in the end system is in the PPR modules and is mounted in separate ATCA shelves. The basic principle is to maintain four racks for the new partitioning (two for the main barrel and two for the extended barrels) each with 8 PPR blades [3].

The FE electronics interface, the pipeline buffering, and signal reconstruction are carried out in the PPR ATCA blade while the TDAQ Interface (TDAQi) Rear Transition Module (RTM) will interface with the Trigger and FELIX. The PPR upgrade module has a full-size ATCA blade design [3].
As mentioned in section 5.6.2, each mini-drawer daughter-board will be connected

to the PPR through. 4 data links and 2 TTC links, such that there is redundancy through the middle of the mini-drawer. Since there are 4 mini-drawers. We therefore, require a total of 12 links per super-drawer side, which can be routed using a single Multi-Fiber Push On (MPO) cable. A second completely redundant MPO fiber is mounted per super-drawer. Optical fibers are single-mode, Optical Multimode Type 3 (OM3) and tolerant to radiation shown in section 5.2. The routing from the detector to the PPR in the electronics room is organized into trunk cables [3]. To reduce latency, the path is as short as possible. Figure 5.13 shows the functional block diagram for the new system.

5.6.5 The TileCal Demonstrator

In order to evaluate and validate the new readout and trigger concepts, an experimental "TileCal demonstrator" (see Figure 5.14) model has been produced in full. The model is based on the 3-in-1 FE design and is completely compatible with the current system, including both analog trigger sum for the existing L1 trigger and digital readout for the PPR trigger prototypes. The PPR is the central part of the off-detector electronics for the demonstrator program. The PPR can be operated in the upgrade and legacy mode; in the legacy mode it emulates the FE electronics. The upgrades and legacy systems run parallel and are synchronised using the clock and trigger data transmitted from the legacy TTC modules via dedicated optical connections. The PPR adds identification information from triggers to data packets which are used at the readout driver level to synchronise [42].

The PPR prototype also implements a readout architecture for the upgrades which is usable in stand-alone mode or parallel to the legacy system. The PPR runs within its legacy infrastructure and transfers the triggered data to the FELIX

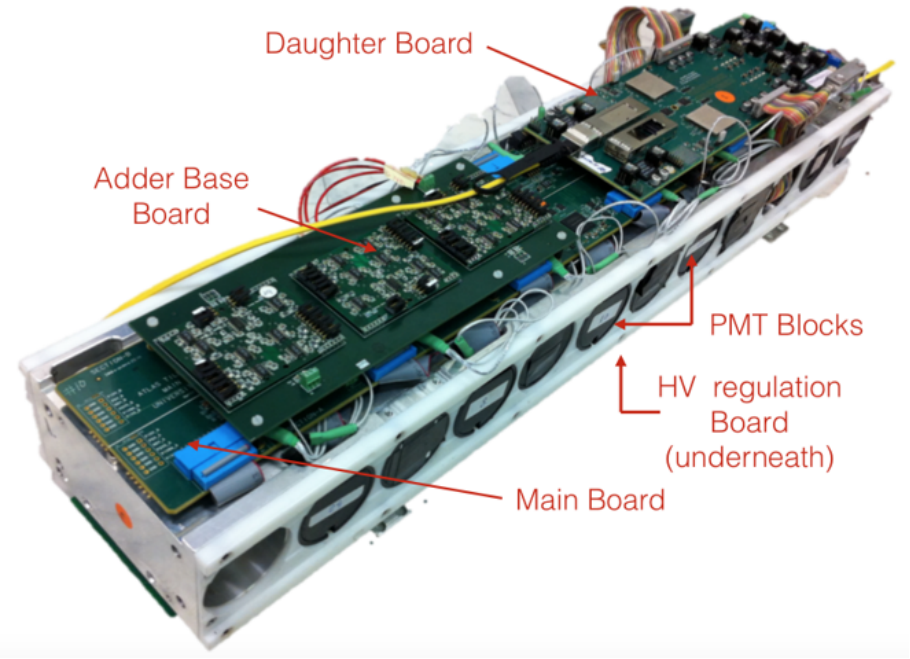
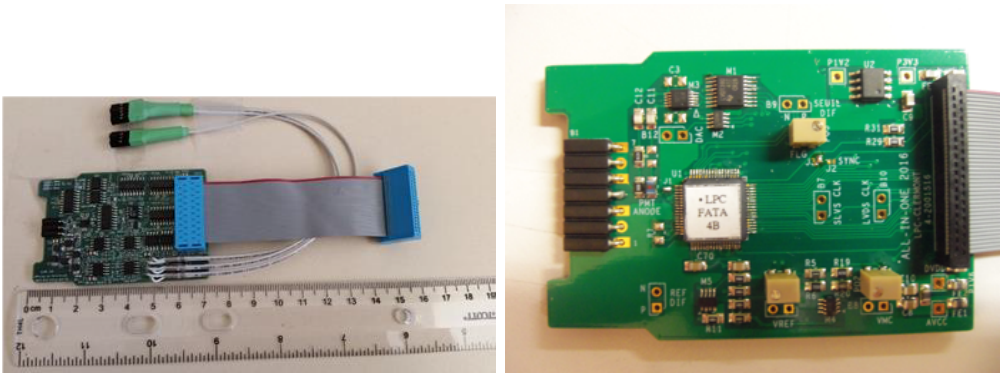


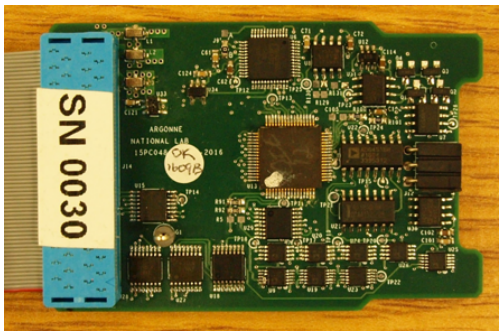
Figure 5.14: The TileCal Demonstrator with the new FE electronics embedded [45].

system via a high-speed optical connection to store its data for offline reconstruction and analysis on a local disk.

During the previous TBs, the prototype TileCal demonstrator was equipped with the legacy and upgraded electronics and the performance of the prototype was tested using different particle beams with different energies. In 2015 two different TB campaigns tested the 3-in-1 solution alone and in 2016 and 2017 the other two experimental FE technologies (A Dedicated FE ASIC for the ATLAS TileCal Upgrade (FATALIC) and Charge Integrator and Encoder (QIE)) were evaluated in addition to the 3-in-1 (see Figure 5.15). The modules were mounted on a remote mobile table to indicate the beam at the various modules and cells and at different angles. The modules have been exposed to different energies of muons, positrons and hadrons. The beam system has been installed for separating the



(a) (b)



(c)

Figure 5.15: The new FE electronics proposed for the upgrades. (a) is the new 3-in-1 option, (b) is the FATALIC card and (c) is the QIE card [30].

various types of particles, measuring the location of the beam, activating the data readout and synchronising the beam. There are two Cherenkov counters used to separate protons, pions and electrons for energies less than 50 GeV, and a muon hodoscope was used to detect muons behind the tubes. The wire chambers of the Cherenkov counters provide the exact position of the beam on the modules, and a coincidence trigger in two scintillator detectors produced the signal [3, 42].

Synchronisation with the TTC system is one of the key integration subjects for the demonstrator. The TTC clock recovery technique tests the discrepancy in phases between the TTC and local signals with a resolution of less than 15 ps. The bench measurements showed a maximum variation delay of less than 100 ps

after 1000 reset cycles while the studies on long-term stability showed a maximum phase difference of 10 ps during 8 hours of operation. Such studies show that the predicted phase variation between the LHC clock transmitted and the receiver is below 100 ps [3].

5.6.6 Calibration Systems

As mentioned in Section 3.3, the calibration systems of TileCal are CIS, Laser and ^{137}Cs. These systems will be upgraded like detailed below.

5.6.6.1 The Charge Injection System

The CIS has been updated in order to keep track with the new 3-in-1 card dynamic range.

5.6.6.2 The Laser System

The Laser System can be upgraded by following the recommendations below:

- The laser source as well as the optical components inside the optics box must be replaced due to aging.
- In order to comply with the TDAQ upgrades, the electronic unit called LASCAR, which manages the laser system and interfaces it with the TDAQ system has to be modified.

5.6.6.3 Cesium System

The Cs control system must be upgraded to be integrated into the ELMB++ of the LVPS system via a mezzanine, or to the Daughter-board through the SPI interface of the GBTX, and thus interfaced through FELIX via the PPR. The two options are still possible [3, 42].

Chapter 6

Test-Beam Campaigns

6.1 Test-Beam Setup

During the Test-Beam (TB) three TileCal modules, two LBs and one EB, were exposed to muons, pions, kaons, electrons and protons with different energies and angles of incidence. The data from September 2017 TB allow the performance of the updated FE electronics systems built for LHC upgrade operations to be examined. The results from the TB data was compared with the simulated data that were obtained using ATLAS offline software simulation framework based on Geant4 [46]. As mentioned in Section 3, the electromagnetic calibration of the TileCal cells was achieved by equalizing the current of the photo-multiplier that was induced by a moving ^{137}Cs radioactive source through each line of the scintillating. Since the response of the tiles depends on the impact point location and size of the tile, correction factors were applied for each cell size. The scale was maintained in ATLAS by adjusting the PMT gain in order to reproduce the PMT current of the reference ^{137}Cs source at the level it had during the electron beam tests, where the calibration factor was set. ATLAS uses the reaction of the simulated electrons to set the energy scale of the MC jets. In the case of good

performance of the FE electronics systems foreseen for the LHC upgrades, the same calibration technique has been applied with the data collected at 2017 TBs and then one expects to get responses to the leptons and hadrons close to those that were obtained by the 2000 TB data analysis [3, 47].

6.1.1 Beam Line and Calorimeter setup

The particle beams were obtained by extracting 400 GeV protons from the Super Proton Synchrotron (SPS) accelerator, made collide with a primary target of beryllium was 300 mm long while the produced secondary beams are allowed to have energies that ranges from 10 GeV to 350 GeV. A secondary target made up of 1000 mm long polyethylene, together with a lead absorber can be positioned inside the beam to produce tertiary beams. The beam momentum and charge is determined by the bending magnets. Other constituents were the electrons, kaons and muons. Figure 6.1 shows the setup of the H8 beamline that is equipped with coincidence trigger scintillators, beam particle identification Cherenkov counters, and wire chambers for lateral beam particle coordinates. The TileCal TB setup (see Figure 6.2) consists of two LB (LBA and LBC) and EB (EBA and EBC) super-drawers. The LB super-drawer LBC 65 is equipped with the 3-in-1 card upgrade option, while the other option the FATALIC card, which is the alternative to the 3-in-1 card is mounted in LBA65. The other super-drawers M0 C and EBC 65 were equipped with the legacy system. The M0 C super-drawer was equipped with Multi-Anode (MA) Photo-Multipliers. For comparison the modules were stacked on a scanning table, which was able to position the modules at any desired angle and location with respect to the input particles. Data was collected from the incident beams at the center of the front of the A-cell at the angle of $\theta = 20^{\circ}$ away from the normal and incident at the ends of the modules, in the center of each tile row. Two selection criteria were generally applied to all particle

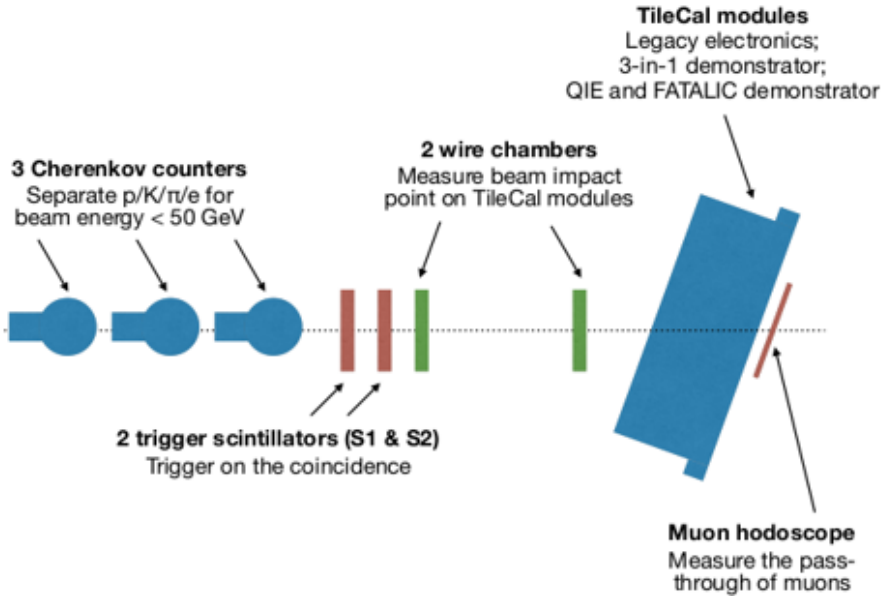


Figure 6.1: Modules and beam elements at the SPS H8 Beam-line [48].

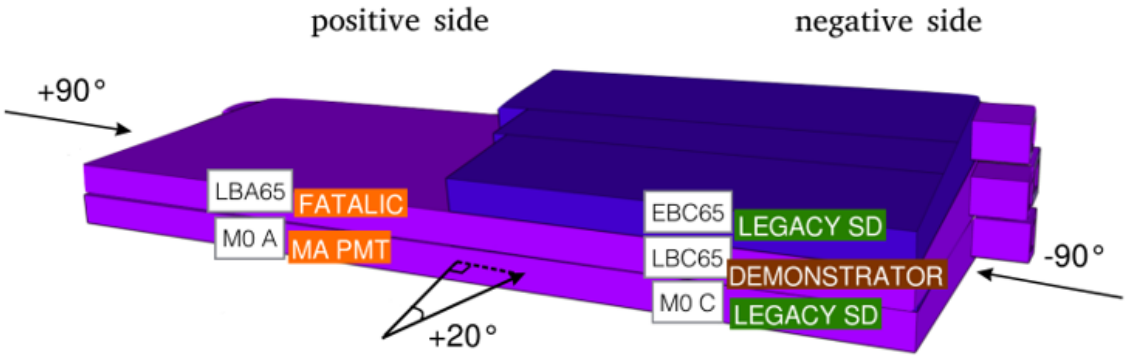


Figure 6.2: The schematic front view of the TileCal Modules placed on the scanning table at the H8 beam [3].

beams. Single-particle events were picked with beam detectors upstream of the TileCal for all particle types. Signals from single minimum ionizing particles were required in the upstream scintillator counters. This cut, particularly suitable for electrons, removes particles that initiated upstream showering of the calorimeter and two-particle events. Events in which the beam chambers displayed tracks far from or outside the beam axis were dismissed as they could scatter upstream and thus be off-energy. The second set of selection criteria was for the particular particle type to be studied. Nevertheless, the three strip-lined cherenkov counters further assisted in the detection of particles with different energy sources, mainly through the calorimeter response [3, 47].

6.2 Test-Beam Results

6.2.1 Results with electrons

The results for electrons are the TileCal TB analysis conducted in 2017 and 2018. The main idea with electrons in particular is to better understand the EM showers that sometimes develop inside the hadronic ones. The TB results on electrons focuses on the response of electrons at energies 20 GeV, 50 GeV and 100 GeV. The initial electron data is contaminated with data from other particles, mainly hadrons. The data of the electrons was yet to be separated from the hadron data. The analysed electron runs with the beam hitting at LB or EB modules in an angle of $\theta = 20^{\circ}$ at different values of E_{beam} and HV settings. The plots in this section were created by the author using ROOT software, taking into account the points with the most interesting events (points where the beam was most visible).

Figure 6.3 shows the beam profiles for the signals in the X impact point (X_{imp})

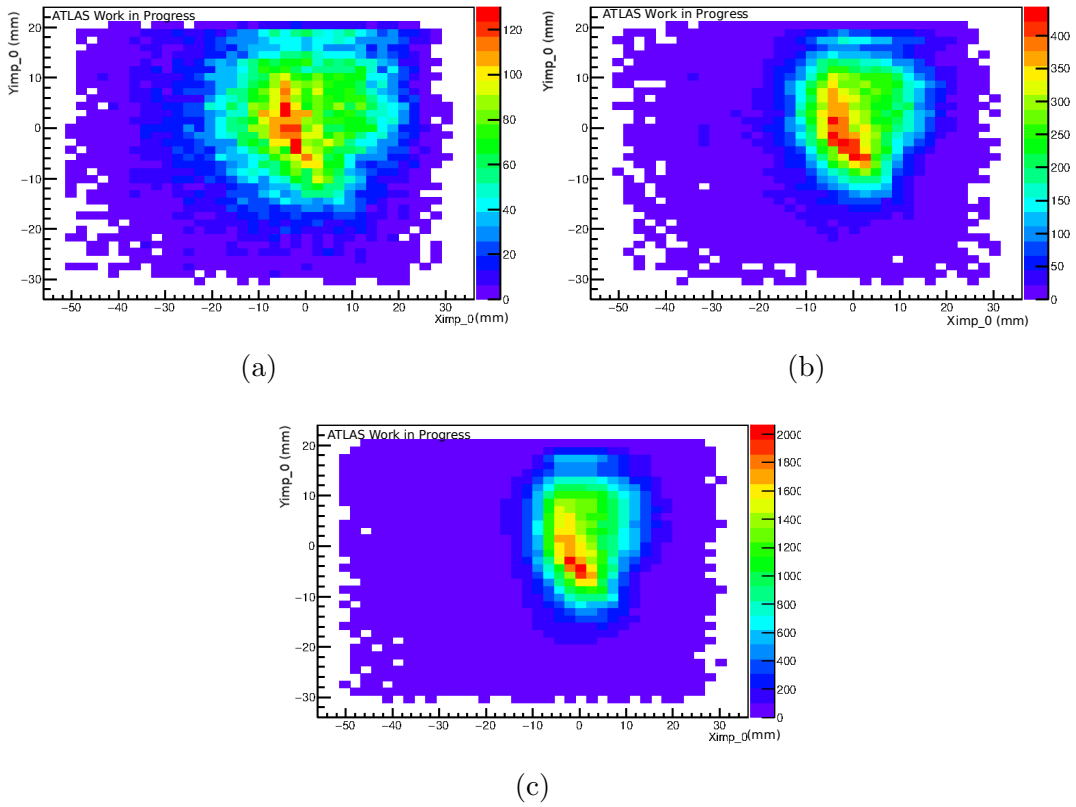


Figure 6.3: Beam Profiles for 20 GeV (a), 50 GeV (b) and 100 GeV (c) electron signals. The data for the plots is from the 2018 TB campaigns.

and Y impact point (Y_{imp}). The X impact point and Y impact point are the coordinate points when the TB table is rotated at angle $\theta = 20°$.
The profile plots show how the beam was mostly distributed and concentrated in the center as expected. The regions with the most visible beam are: $X_{imp} >$ -50 and $X_{imp} <$ 35 and $Y_{imp} >$ -30 and $Y_{imp} <$ 20. It can be seen from the figure that the beam gets more focused as the energy increases. The focus of low energy beams is affected by multiple scattering in the material.

Pure electron signal samples are targeted by separating electrons from other particles (mostly concerned about electron/hadron separation). The electrons were selected using the C_{long} and C_{tot} shower profile parameters, using the difference in the calorimeter between the electromagnetic and the hadronic shower profiles [47]. The C_{long} equation 6.1 corresponds to the energy fraction of the first two longitudinal layers (A,BC,D) of the module (given by index i), and 3 adjacent towers (given by index j):

$$C_{long} = \sum_{i=1}^{2} \sum_{j=1}^{3} \frac{E_{ij}}{E_{beam}}, \tag{6.1}$$

where E_{ij} stands for the measured energy in each cell. The C_{tot} equation 6.2 calculates the spread of the energy shower:

$$C_{tot} = \frac{1}{\sum_c E_c^\alpha} \sqrt{\sum_c \frac{(E_c^\alpha - \frac{\sum_c E_c^\alpha}{N_{cell}})^2}{N_{cell}}}, \tag{6.2}$$

where E_c represents the energy in cell c, and N_{cell}represents the total number of cells considered which in our case is $N_{cell} = 9$. The exponent α= 0.6 was tuned at the TB of 2005 [46] to achieve maximum electron/hadron separation based on MC simulation. Pure electromagnetic showers will have wider lateral spread

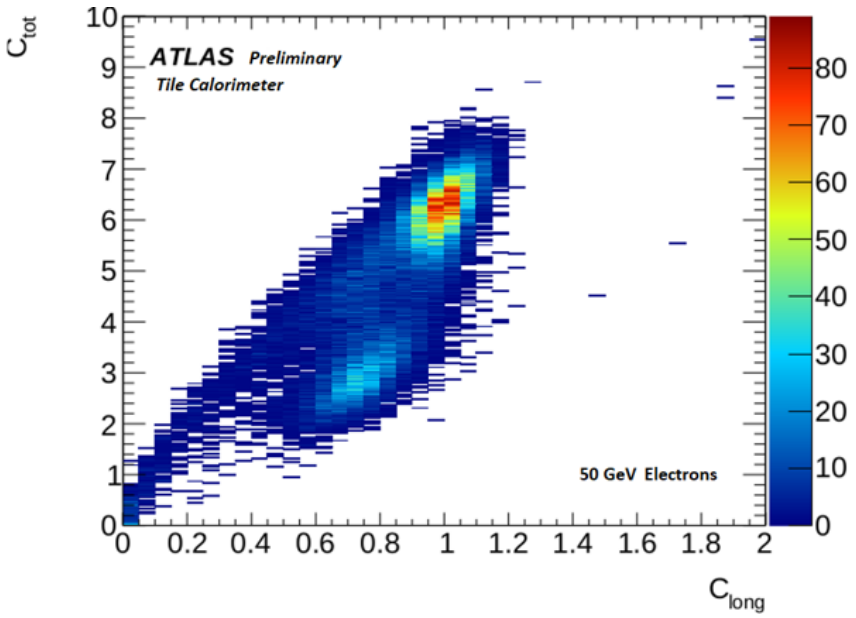


Figure 6.4: The scatter plots shows how the electrons and hadrons at 50 GeV are separated using the C_{tot} vs C_{long} method. The region to the right/top is the electron, the other the hadron [49].

(C_{long}), and larger overall spread (C_{tot}) in the TileCal which has ∼14 X0 and only ∼1.5 λ in the first layer.

Figure 6.4 shows the C_{long} vs C_{tot} scatter plot that shows how the separation takes place. The two variables provide effective electron/hadron separation when used together. The top part on the figure refers to the electrons while the other is the hadrons. The C_{long} (C_{tot}) cut varies from 0.75 (2.1) at 20 GeV to 0.88 (6.5) at 100 GeV, depending on beam energy [3, 48]. At energy E$beam$ = 20 GeV, the purity of the electron sample is increased as the signal from the Cherenkov counters 1 and 3 of the beam line is greater than 500 ADC counts [48, 50].

The Figures 6.5 and 6.6 show the C_{long} and C_{tot} plot distributions (respectively) for the electron energy signal at 20 GeV, 50 GeV and 100 GeV. The vertical lines

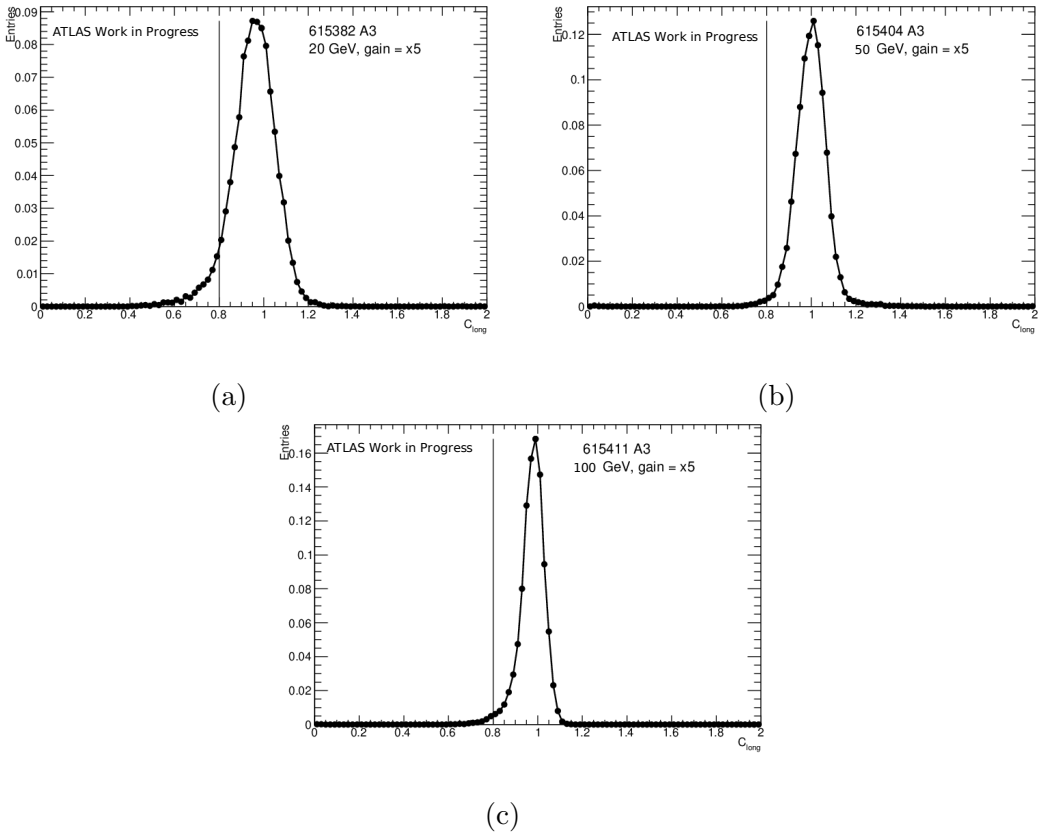


Figure 6.5: The C_{long} (a) plot distribution for the electron signal at 20 GeV (a), 50 GeV (b) and 100 GeV (c).

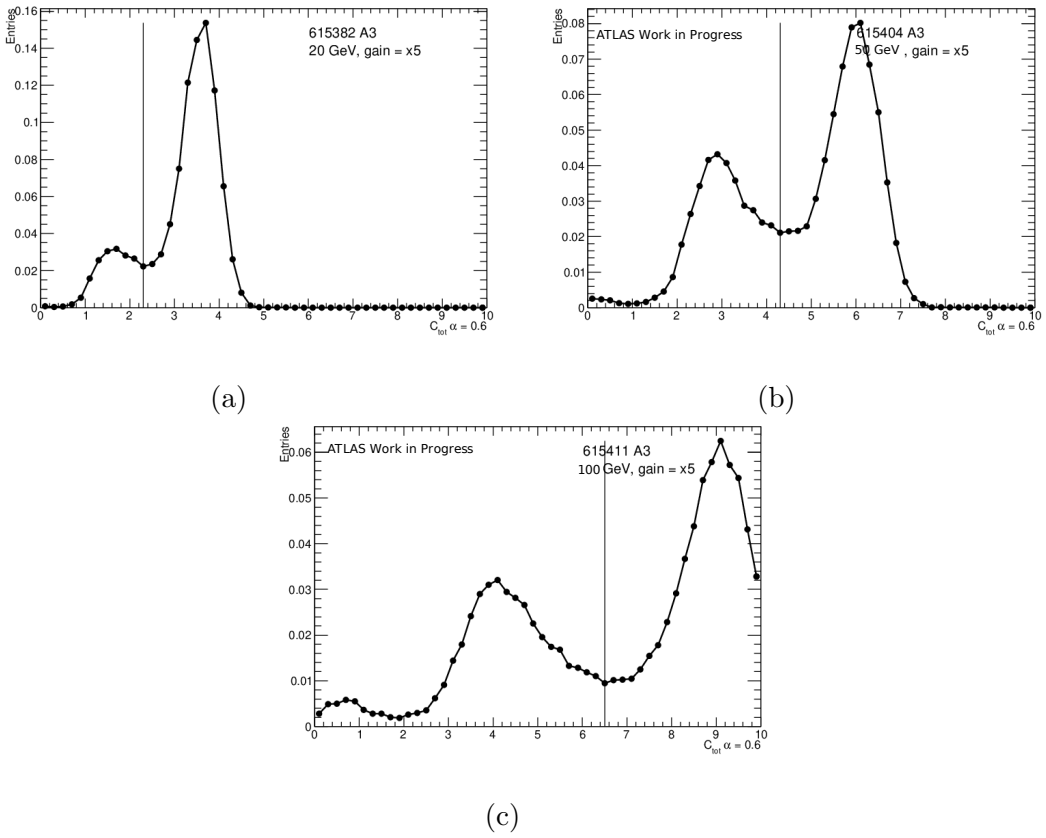


Figure 6.6: The C_{tot} plot distribution for the electron signal at 20 GeV (a), 50 GeV (b) and 100 GeV (c).

on the plots shows the points where the cuts are supposed to be made. In Figure 6.5 the cut for the 20 GeV signal is made at $C_{long} \sim 0.8$ and $C_{tot} \sim 2.4$, while the cut for 50 GeV signal is also made at $C_{long} \sim 0.8$ and $C_{tot} \sim 4.5$ and for the 100 GeV the cut at $C_{long} \sim 0.8$ and $C_{tot} \sim 6.6$. It can be assumed that the data on the left side of the vertical line is that of the hadrons, while the data on the right side are the electrons. It can be observed that on the C_{tot} the cuts on all the plots is made just before the highest peak which moves further along the x-axis as the energy increases. The value of α has no significant influence on the variable performance.

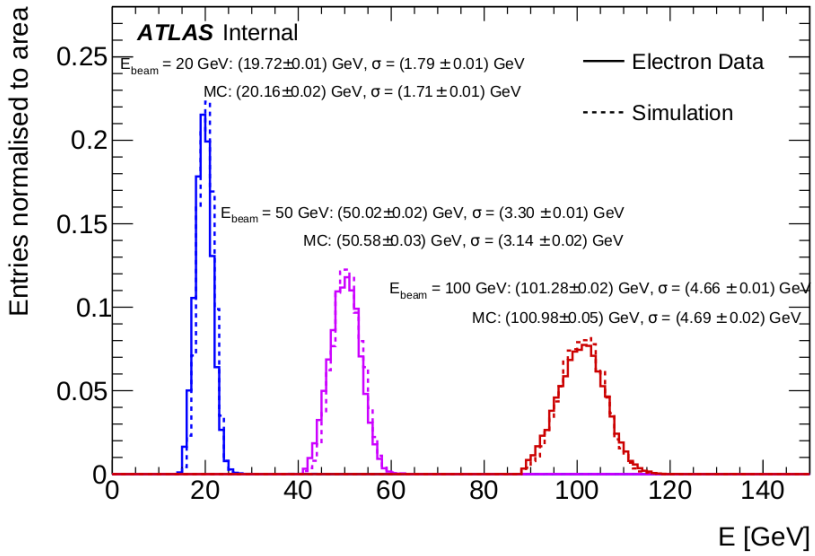
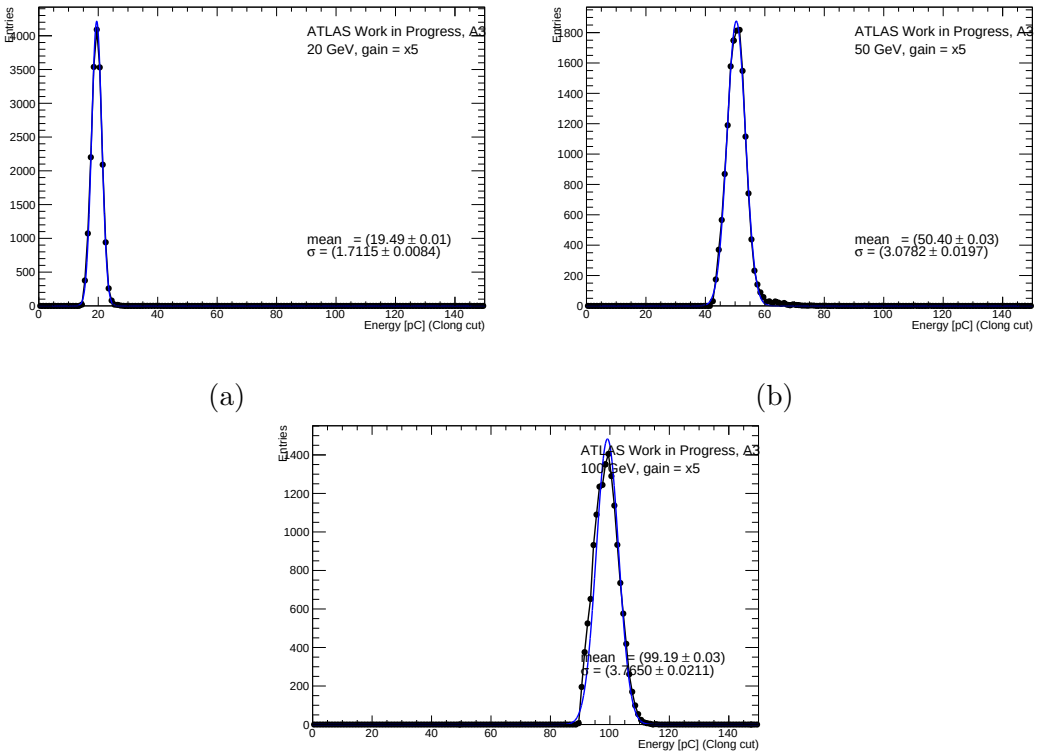


Figure 6.7: The Total energy deposited in the calorimeter 20 GeV , 50 GeV and 100 GeV electrons incident in the cell A4 at 20° and simulated results using Geant 4.10.1 Fritiof model implemented inside Geant4 (FTFP) and Bertini Cascade (BERT) [48].

Figure 6.7 shows the simulated data for the electrons in the cell A4 at $\theta = 20°$. The data has to correspond to the simulated data before the new electronics are verified (The cell area does not matter). In the case of an electron beam, the full energy of the electromagnetic can be collected, and the peak of the distribution will coincide with the energy of the beam.

Figure 6.8 shows the pure electron signal plots at energies of 20 GeV, 50 GeV and 100 GeV. The figure shows the appearance of the electron data without any contamination from the hadron data. Pure electron plots are easier to analyse and are compared to previous TB data where current electronics have been used.

Since the tiles are placed perpendicularly to the beam direction, the sampling fraction of the shower will depend on the incident beam position. If the beam



(a) (b)

(c)

Figure 6.8: Pure Electron signal plots at 20 GeV (a), 50 GeV (b) and 100 GeV (c) after separation from other particles.

hits first the scintillator tiles the measured energy will he higher that if it hits the absorber steel plates, as shown in Figure 6.9. The energy dependence with the position (X) is well described by a simple regular function:

$$E_{raw}(X) = p_0[1 + p_1 sin(\frac{2\pi X}{p_2} + p_3)], \tag{6.3}$$

where p_0 is equivalent to the average energy and is used to evaluate the calibration constant:

$$E_{fit} = p_0. \tag{6.4}$$

The parameter p_1 indicates the oscillation's relative amplitude. The parameter p_2 is the thickness of the time as seen by the beam at the angle of impact of 200 and p_3 is a phase. The impact point X is redeveloped with the chambers of the beam [3].

As shown in Figure 6.10, where the E_{fit}/E_{beam} is plotted as a function of the beam energy, the uncertainty of the calibration constant is less than 4% for the 3 beam energies considered. This is expected to improve with increased statistics.

6.2.2 Results with Muons

Muons produced in the H8 beam line, are minimum ionizing particles, they deposit a constant amount of energy along their path through matter and independently of the angle of incidence, they traverse all the TileCal modules. Therefore, the measurement was carried out by rotating the TileCal by $\theta = 90°$, so that the beam would cross completely the modules completely perpendicular to the tiles, and parallel to the beam in ATLAS. Beam was pointed to the center of each of the 11 rows of tiles in the radial direction with an energy of 165 GeV [3, 48, 51].

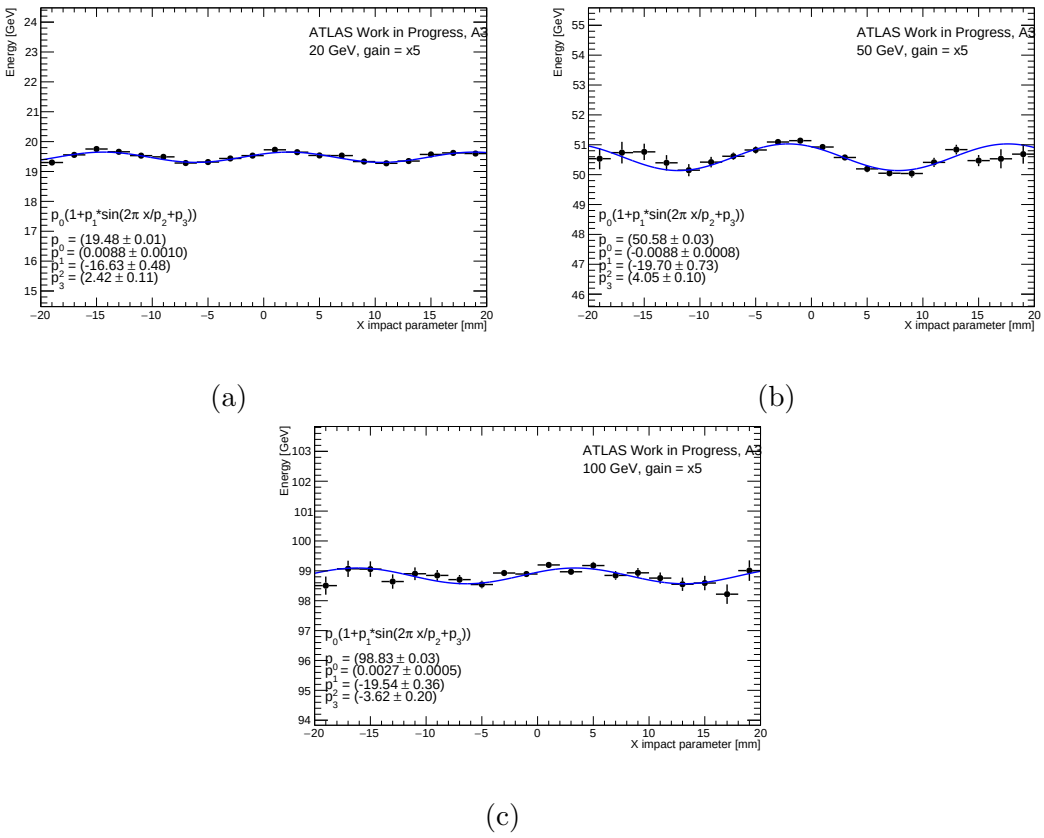


Figure 6.9: The oscillation of the electron response by the difference in the sample fractions determined by 20 GeV (a), 50 GeV and 100 GeV beam signal. The line indicates the correction for the consequence of Equation 6.3.

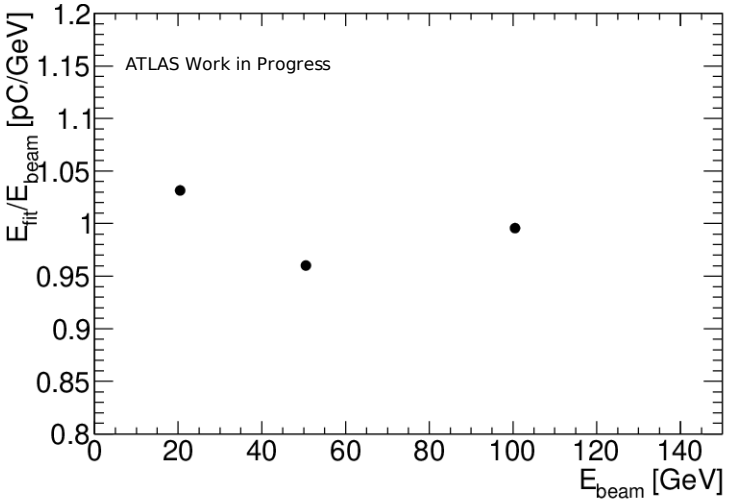


Figure 6.10: Calibration constant from pC to GeV represented as E_{fit}/E_{beam}, for electron beam energies of 20 GeV, 50 GeV and 100 GeV.

Figure 6.11 show the muon response in the wire chambers in the beam line (cha1 and cha2). From the figure it can be observed that cha1 has a better beam response than cha2. X_{imp} and Y_{imp} refers to the coordinates of the beam at point of impact. The points with the most visible beam are: Xcha1, Xcha2, $X_{imp}, >$ -50 and Xcha1, Xcha2, $X_{imp} <$ 35 and Ycha1, Ycha2, $Y_{imp} >$ -30 and Ycha1, Ycha2, $Y_{imp} <$ 20.

Figure 6.12 shows the muon response in the wire chambers in the beamline (cha1 and cha2) for the 300 GeV muon signal. From the figure it can be observed that cha1 has a better beam response than cha2. X_{imp} and Y_{imp} refers to the coordinates of the beam at point of impact. These beam quality and the maximum precision of the data can be inferred from these plots.

The response of the TileCal to high-energy muons is a Landau distribution with typically long tails at high energies. The Total energy is obtained as the sum of

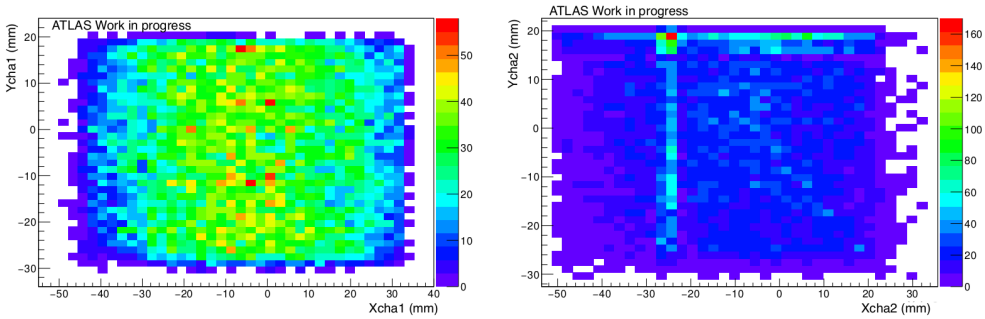


Figure 6.11: The two plots (a) and (b) show the beam response in chambers 1 and 2 for 165 GeV muons. They show how the beam is distributed in each chamber. The bottom plots show the beam at the impact point.

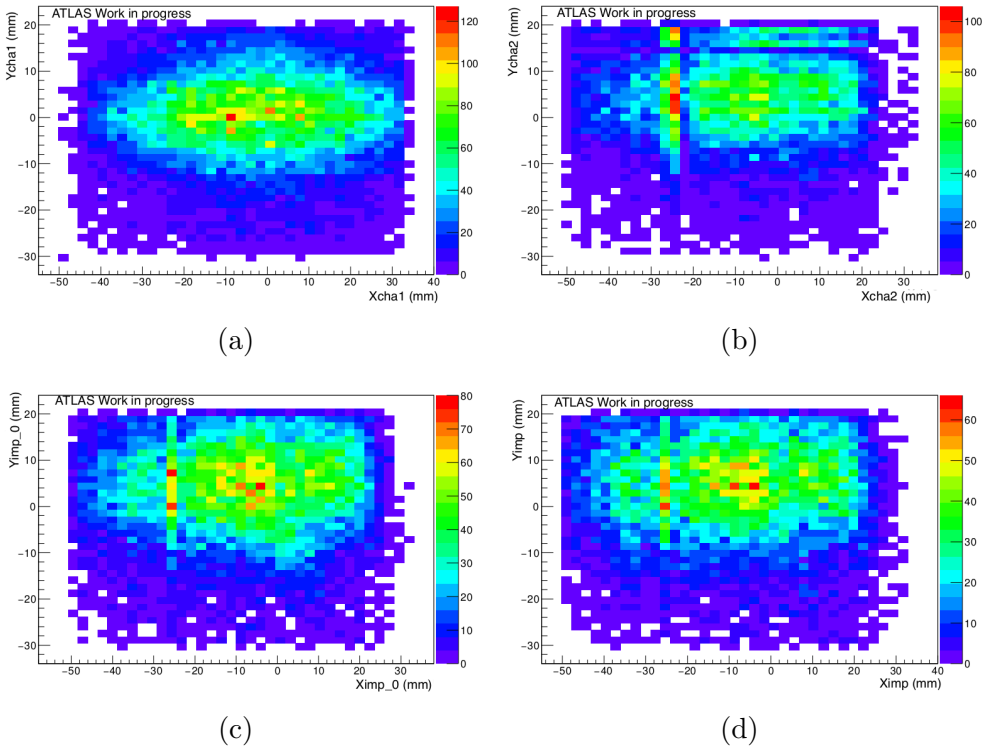


Figure 6.12: The two plots (a) and (b) at the top shows the beam response in chambers 1 and 2 for the 300 GeV muons. They show how the beam is distributed in each chamber. The bottom plots (c) and (d) shows the beam at the point of impact.

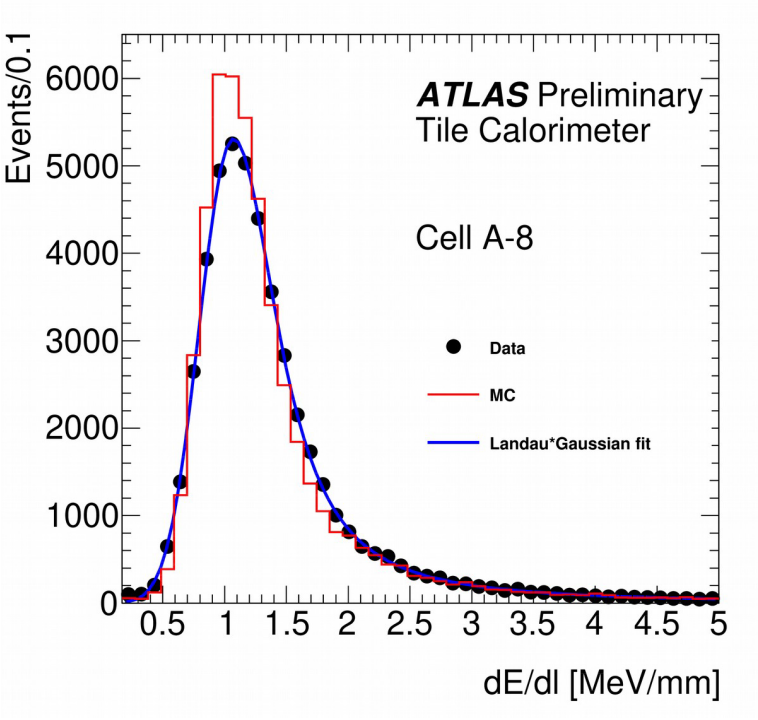


Figure 6.13: Distribution of dE/dl using experimental data and simulated muons at θ -90° [51].

the reconstructed energy in each PMT of a cell [51]. Three types of tiles at the TB surface were irradiated by muon beam at different points: Tile 2 (165 GeV), Tile 6 (300 GeV), Tile 10 (300 GeV)

Figure 6.13 shows the distribution of dE/dl using experimental data and simulated muons at θ = -90° and an energy of 165 GeV. The muon data from the TB is compared to this distribution plot to further verify the functionality of the new electronics.

6.2.3 Performance of the FE electronics

The performance of the new electronics proposed for the upgrades is determined during the TB periods. The data obtained from the TBs have to match with the simulations and the data from the current electronics acquired in the TB of year 2005. The analysis of the electron and muon data yields very good results, consistent with the previous results within 4%. Additional analysis from the wire chambers yield a small beam profile used for this TB campaign.

Chapter 7

Conclusions

As ATLAS is undergoing the LS2 and the TileCal electronics are currently under maintenance in preparation for the upcoming data-taking period (Run 3). During this maintenance period, two electronics functionality testing systems are being used to validate the repairs (MobiDICK and DVS). However, while the DVS tests are designed to be identical to the MobiDICK tests, but to be executed with the ATLAS online software and BE readout electronics once the super-drawer is in its final position, occasionally, after a drawer repair, the offline team might receive negative feedback about certain faults that are not identified by DVS and MobiDICK. This shows that more DVS tests need to be implemented to deal with such issues. There are currently more DVS tests being implemented to be able to improve the quality assurance procedure after the repairs. In particular, a stuckbit test is currently being implemented by the author, which is currently not available in DVS but it is in MobiDICK.

Furthermore, in view of the HL upgrade of the LHC, TileCal is undergoing TB campaigns that aim at testing the performance of the new electronics that are deemed to be compatible with the HL-LHC. The new proposed electronics were embedded in the prototype TileCal module, the demonstrator. In the TB cam-

paigns between 2017 and 2018, these modules have been equipped with the electronic update with modules fitted with a legacy system that shows different particles and energies from the SPS accelerator. The TB data analysis in this paper is performed for the demonstrator program during the 2017-2018 TB period. The data analysis performed is related to the electrons and the muons. The data from the electrons and muons allow for the verification of the performance of the new electronics. The results achieved with muons and electrons are consistent with the settings for calibration obtained with the old electronics and with the expectations produced by simulated data. The results show that the new electronics are performing well.

References

[1] L. Evans and P. Bryant, "LHC Machine," *Journal of Instrumentation*, vol. 3, pp. S08001–S08001, August 2008.

[2] ATLAS Collaboration, "ATLAS Tile calorimeter: Technical Design Report," Tech. Rep. CERN-LHCC-96-042. ATLAS-TDR-3, Geneva, 1996.

[3] ATLAS Collaboration, "Technical Design Report for the Phase-II Upgrade of the ATLAS Tile Calorimeter," Tech. Rep. CERN-LHCC-2017-019. ATLAS-TDR-028, CERN, Geneva, September 2017.

[4] CERN, "The Large Hadron Collider," Date accessed: 27.06.2019 from https://home.cern/science/accelerators/large-hadron-collider.

[5] M. Aaboud *et al.*, "Reconstruction of primary vertices at the ATLAS experiment in Run 1 proton–proton collisions at the LHC," *The European Physical Journal C*, vol. 77, p. 332, May 2017.

[6] F. Englert and R. Brout, "Broken symmetry and the masses of gauge vector mesons," *Phys. Rev. Lett.*, vol. 13, pp. 321–323, 1964.

[7] P. Higgs, "Broken Symmetries and the Masses of Gauge Bosons," *Phys. Rev. Lett.*, vol. 13, pp. 508–509, Oct 1964.

[8] CERN, "LHC collides ions at new record energy," November 2015.

[9] A. Georges *et al.*, "Technical Design Report for the Phase-I Upgrade of the ATLAS TDAQ System," Tech. Rep. CERN-LHCC-2013-018. ATLAS-TDR-023, September 2013. Final version presented to December 2013 LHCC.

[10] E. Mobs, "The CERN accelerator complex - 2019. Complexe des accélérateurs du CERN - 2019," Jul 2019. General Photo.

[11] CERN, "Detector and Technology," Date accessed: 25.08.2019. https://atlas.cern/discover/detector.

[12] ATLAS Collaboration, "The ATLAS Experiment at the CERN Large Hadron Collider," *Journal of instrumentation*, vol. 3, pp. S08003–S08003, August 2008.

[13] D. Primor, *Local tracking in the ATLAS muon spectrometer*. PhD thesis, Tel Aviv U., 2007.

[14] ATLAS Collaboration, *ATLAS Inner Detector:Technical Design Report, 1.* Technical Design Report ATLAS, CERN, April 1997.

[15] ATLAS Collaboration, *ATLAS Detector and Physics Performance: Technical Design Report, 1.* Technical Design Report ATLAS, CERN, May 1999.

[16] E. Stanecka, "THE ATLAS Inner Detector Operation, Data Quality and Tracking Performance.," pp. 383–388, March 2013. Proceeding of Physics in Collision, Slovakia, arXiv:1303.3630.

[17] N. Buchanan *et al.*, "Design and implementation of the Front End Board for the readout of the ATLAS liquid argon calorimeters," *Journal of Instrumentation*, vol. 3, p. P03004, March 2008.

[18] ATLAS Collaboration *et al.*, "Construction, assembly and tests of the ATLAS electromagnetic end-cap calorimeters," *Journal of Instrumentation*, vol. 3, p. P06002, June 2008.

[19] A. Georges *et al.*, "Readiness of the ATLAS Tile Calorimeter for LHC collisions," *European Physical Journal C*, January 2010.

[20] J. Archambault *et al.*, "Performance of the ATLAS liquid argon forward calorimeter in beam tests," *Journal of Instrumentation*, vol. 8, p. P05006, May 2013.

[21] ATLAS Experiment and O. Kortner, "Muon Performance Public Figures from Simulation," January 2009.

[22] A. Wilkins, "Upgrades to ATLAS and LHC Magnets for Run 2 and Beyond," July 2015. https://www.bnl.gov/newsroom/news.php?a=25764.

[23] ATLAS TDAQ Collaboration, "The ATLAS Data Acquisition and High Level Trigger system," *Journal of Instrumentation*, vol. 11, pp. P06008–P06008, June 2016.

[24] A. Krasznahorkay, "The evolution of the Trigger and Data Acquisition System in the ATLAS experiment," Tech. Rep. ATL-DAQ-PROC-2013-018, CERN, Geneva, September 2013.

[25] C.A. Solans Sánchez, "Implementation of the ROD Crade DAQ Software for the ATLAS Tile Calorimeter and a Search for MSSM Higgs Boson Decaying into Tau Pairs," p. 266, November 2010. CERN-THESIS-2010-162, University of Valencia.

[26] T. Colombo, "Data-flow Performance Optimisation on Unreliable Networks:

the ATLAS Data-Acquisition Case," *Journal of Physics: Conference Series*, vol. 608, p. 012005, May 2015.

[27] A.R. Martínez, "The Run-2 ATLAS Trigger System," *Journal of Physics: Conference Series*, vol. 762, p. 012003, October 2016.

[28] R. Spiwoks *et al.*, "The ATLAS Level-1 Central Trigger." Presentation, September 2007.

[29] S.R. Armstrong *et al.*, "An Overview of Algorithms for the ATLAS High Level Trigger," Tech. Rep. ATL-CONF-2003-003. ATL-DAQ-2003-029. 3, CERN, Geneva, June 2003. revised version number 1 submitted on 2003-06-26 14:59:28.

[30] D.R. Hlaluku, "ATLAS Tile Calorimeter Online Software Reorganization and Phase-II test-beam campaigns." MSc Thesis, 2017.

[31] V. Giangiobbe and D. Calvet, "Performance of the TileCal super-drawers from a global analysis of the MobiDICK tests," Tech. Rep. ATL-TILECAL-PUB-2008-007. ATL-COM-TILECAL-2007-010, CERN, Geneva, April 2007.

[32] D.E. Boumediene, "Calibration and monitoring of the ATLAS Tile calorimeter," Tech. Rep. ATL-TILECAL-PROC-2017-022, CERN, Geneva, November 2017.

[33] J. Carvalho, "Calibration and monitoring of the ATLAS Tile calorimeter," Tech. Rep. ATL-TILECAL-PUB-2006-007. ATL-COM-TILECAL-2006-009. CERN-ATL-COM-TILECAL-2006-009, CERN, Geneva, July 2006.

[34] The ATLAS Tile Calorimeter System, "TileDVSUser twiki page," 2019. Date Accessed: 20-09-2019.

[35] I. Soloviev *et al.*, "Verification and Diagnostics Framework in ATLAS Trigger/DAQ," Tech. Rep. ATL-DAQ-2003-033, CERN, Geneva, May 2003.

[36] F. Carrió *et al.*, "Design of an FPGA-based embedded system for the ATLAS Tile Calorimeter front-end electronics test-bench," *Journal of Instrumentation*, vol. 9, February 2014.

[37] N. Lekalakala, T. Masuku and B. Mellado, "The Diagnostic and Verification System for the Tile Calorimeter Trigger and Data Acquisition framework of the ATLAS Detector." Submitted to Proceedings of SAIP2019, 64^{th} Annual Conference of the South African Institute of Physics, 2019.

[38] C. Pralavorio, "Record luminosity: well done LHC," November 2017.

[39] CERN, "A new schedule for the LHC and its successor," Date Accessed: 13-12-2019 https://home.cern/news/news/accelerators/new-schedule-lhc-and-its-successor.

[40] G. Usai, "ATLAS Tile Calorimeter electronics and future upgrades," *Journal of Instrumentation*, vol. 10, pp. C04026–C04026, April 2015.

[41] "HL-LHC Industry - Project Schedule," Date Accessed: 26.10.2020. https://project-hl-lhc-industry.web.cern.ch/content/project-schedule.

[42] ATLAS Collaboration, "Letter of Intent for the Phase-II Upgrade of the ATLAS Experiment," Tech. Rep. CERN-LHCC-2012-022. LHCC-I-023, December 2012.

[43] A. Solodkov, "Upgrade of the ATLAS hadronic Tile Calorimeter for the High luminosity LHC," *Journal of Instrumentation*, vol. 12, pp. C08004–C08004, August 2017.

[44] F. Scuri, "Upgrade of the ATLAS Tile Calorimeter for the High Luminosity LHC," *Journal of Physics: Conference Series*, vol. 1162, p. 012017, January 2019.

[45] A. Valero, "Data acquisition and processing in the ATLAS tile calorimeter phase-II upgrade demonstrator," *Journal of Physics: Conference Series*, vol. 898, p. 032012, October 2017.

[46] S. Agostinelli *et al.*, "Geant4—a simulation toolkit," *Nuclear Instruments and Methods in Physics Research Section A: Accelerators, Spectrometers, Detectors and Associated Equipment*, vol. 506, no. 3, pp. 250 – 303, 2003.

[47] P. Adragna *et al.*, "Testbeam Studies of Production Modules of the ATLAS Tile Calorimeter," *Nucl. Instrum. Methods Phys. Res., A*, vol. 606, pp. 362 – 394, February 2009.

[48] T. Zakareishvili, "Studies of the ATLAS hadronic Calorimeter response to different particles at Test Beams," Tech. Rep. ATL-TILECAL-SLIDE-2018-045, January 2018.

[49] V. Santurio and ATLAS Tile Collaboration, "Beam Tests on the ATLAS Tile Calorimeter Demonstrator Module," Tech. Rep. ATL-TILECAL-PROC-2018-001, CERN, Geneva, June 2018.

[50] N. Lekalakala, T. Masuku and B. Mellado, "Overview of test beam campaigns for readout electronics of the upgrade Tile Calorimeter of the ATLAS Detector." To appear in the book of Proceedings of HEPP2019, the High Energy Particle Physics workshop, 2019.

[51] T. Zakareishvili, "Muon Signals at a Low Signal-to-Noise Ratio Environment," Tech. Rep. ATL-COM-TILECAL-2017-003, CERN, Geneva, January 2017. Workshop BTTB starts at 24th of January, 2017.

[52] V. Baranov, Yu.I. Davydov, R. Erasmus, C.O. Kureba, N. Lekalakala, T. Masuku, J.E. Mdhluli, B. Mellado, G. Mokgatitswane, E. Sideras-Haddad, I. Vasilyev and P.N. Zhmurin, "Effects of neutron radiation on the optical and structural properties of blue and green emitting plastic scintillators," *Nuclear Instruments and Methods in Physics Research Section B: Beam Interactions with Materials and Atoms*, vol. 436, pp. 236 – 243, 2018.

[53] G. Mokgatitwane, B. Mellado, E. Sideras-Haddad, R. Erasmus, T. Masuku, J.E Mdhuli, N. Lekalakala, C.O Kureba, L. Mashishi, G. Peters and T. Sechogela, "A systematic study of the properties of proton induced damage in plastic scintillators for the upgrade of the Tile Calorimeter of the ATLAS detector." February 2019.

[54] CERN, "Taking a closer look at LHC," Date accessed: 20.08.2019.

[55] ATLAS and CMS collaboration, "The Higgs boson," January 2014.

[56] P. Astigarraga and M. Eukeni, "THE ATLAS Data Acquisition System in LHC Run 2," Tech. Rep. ATL-DAQ-PROC-2017-043, CERN, Geneva, Nov 2017.

[57] P. Moreno *et al.*, "A new portable test bench for the ATLAS Tile Calorimeter front-end electronics," vol. 8, pp. C02046–C02046, February 2013.

[58] A. Valero and ATLAS Tile Collaboration, "A new read-out architecture for the ATLAS Tile Calorimeter Phase-II Upgrade," Tech. Rep. ATL-TILECAL-PROC-2015-025, CERN, Geneva, December 2015.

[59] F. Carrio *et al.*, "The PreProcessors for the ATLAS Tile Calorimeter Phase II Upgrade," Tech. Rep. ATL-TILECAL-PROC-2015-021, CERN, Geneva, November 2015.